UNIVERSIDADE ESTADUAL PAULISTA
"JÚLIO DE MESQUITA FILHO"
Campus de Ilha Solteira

**UNIVERSIDADE ESTADUAL PAULISTA "JÚLIO DE MESQUITA FILHO"**

**CAMPUS DE ILHA SOLTEIRA**

**DEPARTMENT OF ELECTRICAL ENGINEERING**

**STEPHANY DE SOUZA LYRA**

# CLOSED LOOP INTERFEROMETRY: INNOVATIVE PROPOSALS FOR OPTICAL PHASE DETECTION BY USING MODERN CONTROL APPROACHES

**Ilha Solteira**
**2022**

**STEPHANY DE SOUZA LYRA**

# CLOSED LOOP INTERFEROMETRY: INNOVATIVE PROPOSALS FOR OPTICAL PHASE DETECTION BY USING MODERN CONTROL APPROACHES

Thesis presented to the post-graduation course of the Engineering Faculty of Ilha Solteira – FEIS – UNESP to obtain the PhD grade in Electrical Engineering.

Specialty: Automation.

Advisor: Prof. Dr. Cláudio Kitano

Co-Advisor: Prof. Dr. Marcelo C. Minhoto Teixeira

Ilha Solteira

2022

FICHA CATALOGRÁFICA
Desenvolvido pelo Serviço Técnico de Biblioteca e Documentação

L992c

Lyra, Stephany de Souza.
Closed loop interferometry: innovative proposals for optical phase detection by using modern control approaches / Stephany de Souza Lyra. -- Ilha Solteira: [s.n.], 2022
85 f.

Tese (doutorado) - Universidade Estadual Paulista. Faculdade de Engenharia de Ilha Solteira. Área de conhecimento: Automação, 2022

Orientador: Cláudio Kitano
Coorientador: Marcelo Carvalho Minhoto Teixeira
Inclui bibliografia

1. Interferometria óptica. 2. Controle moderno. 3. Filtro ressonante. 4. Estrutura variável e modos deslizantes.

Raiane da Silva Santos
Supervisora Técnica de Seção
Seção Técnica de Referência, Atendimento ao usuário e Documentação
Diretoria Técnica de Biblioteca e Documentação
CRB8 - 9999

unesp

**UNIVERSIDADE ESTADUAL PAULISTA**

**Câmpus de Ilha Solteira**

## CERTIFICADO DE APROVAÇÃO

TÍTULO DA TESE: Closed loop interferometry: innovative proposals for optical phase detection by using modern control approaches

**AUTORA: STEPHANY DE SOUZA LYRA**
**ORIENTADOR: CLAUDIO KITANO**
**COORIENTADOR: MARCELO CARVALHO MINHOTO TEIXEIRA**

Aprovada como parte das exigências para obtenção do Título de Doutora em ENGENHARIA ELÉTRICA, área: Automação pela Comissão Examinadora:

Prof. Dr. MARCELO CARVALHO MINHOTO TEIXEIRA (Participaçao Virtual)
Departamento de Engenharia Elétrica / Faculdade de Engenharia de Ilha Solteira - UNESP

Prof. Dr. RICARDO TOKIO HIGUTI (Participaçao Virtual)
Departamento de Engenharia Eletrica / Faculdade de Engenharia de Ilha Solteira - UNESP

Prof. Dr. RODRIGO CARDIM (Participaçao Virtual)
Departamento de Engenharia Elétrica / Faculdade de Engenharia de Ilha Solteira - UNESP

Prof. Dr. JOÃO MARCOS SALVI SAKAMOTO (Participaçao Virtual)
Departamento de Ciência e Tecnologia Aeroespacial / Instituto de Estudos Avançados - IEAv

Prof. Dr. GILDER NADER (Participaçao Virtual)
Centro de Metrologia de Fluidos / Instituto de Pesquisas Tecnológicas do Estado de São Paulo

Ilha Solteira, 04 de fevereiro de 2022

# Dedico

Aos meus avós pelas raízes de nossa natureza. A meus pais, Del e Mônica, pelo fundamento que me manteve. À minha irmã pelas inúmeras distrações. Ao meu companheiro, Alexsson, por sempre me lembrar de ter um pouco mais de fé. Sem vocês, eu não teria conseguido.

# AGRADECIMENTOS

Agradeço a Deus todos os dias pela força e coragem para encarar os desafios desta vida, fé para não desistir e alegria por todas as bênçãos.

Aos meus pais, Mônica e Del, a minha irmã, Sabrina, e ao amor da minha vida, Alexsson, por todo apoio e suporte, que me fizeram chegar até aqui.

Ao meu orientador, Prof. Dr. Cláudio Kitano, pelo exemplo e dedicação, como professor e incentivador.

Ao Prof. Dr. Marcelo Carvalho Minhoto Teixeira pelas ideias mirabolantes, que inspiraram este trabalho.

Ao técnico Everaldo L. de Moraes por todo suporte nos experimentos malucos do LOE.

A meus colegas do laboratório, Guilherme, Perdido e João Paulo, que me ajudaram de toda a forma, e que trabalhando em conjunto fizeram chegar mais longe. Obrigada pela amizade e pelos ‘cafésis’!

E ao CNPq (Processo 140058/2019-2), pelo apoio financeiro que foi essencial para este trabalho.

“Once we accept our limits, we go beyond them.”
– Albert Einstein.

# ABSTRACT

In this work we present a nonlinear control system applied to the two beam optical interferometer, operating with high gain approach (full compensation of interferometric phase), in order to convert the interferometric characteristic curve to a linear characteristic and eliminate complex algorithms for optical phase demodulation (which can involve phase unwrapping methods). The highlight of this work is the use of resonant filter within the controller, is a new proposal that brings together two powerful tools of the nonlinear control: the resonant filter and variable structure. The variable structure has been proved to be an important tool as well as efficient and robust enough to stabilize the interferometer. Also, the structure of the filter allows working with a considerable smaller gain when working in resonance, when compared to previous works. The controlling system was tested on the quadrature interferometer in open loop using a virtual feedback interferometer controlled, which gives equivalence of the physical feedback. This method of implementation was chosen due the need of higher sampling rate and to avoid a greater delay. The system proposed was also studied by changing the controller input (with and without switching, the variable structure, and changing the switching from a sign function to a sigmoidal one). After the experimental test, a piezoelectric flextensional actuator was evaluated under all the variations of the system proposed, and then compared under the same measurement to the arc tangent classical method and the discrepancy between methods in a range of 1,000 Hz was less than 5%, thereby the system developed is validated for measurements of optical phase.



K**ey-words:** optical interferometry; high gain approach; resonant filter; nonlinear control.

# RESUMO

Neste trabalho apresentamos um sistema de controle não linear aplicado ao interferômetro óptico de dois feixes, operando com abordagem de alto ganho (compensação total de fase interferométrica), a fim de converter a curva característica interferométrica para uma característica linear e eliminar algoritmos complexos para demodulação óptica de fase (que pode envolver métodos de desdobramento de fase). O destaque deste trabalho é o uso do filtro ressonante dentro do controlador, é uma nova proposta que reúne duas poderosas ferramentas do controle não linear: o filtro ressonante e a estrutura variável. A estrutura variável provou ser uma ferramenta importante, eficiente e robusta o suficiente para estabilizar o interferômetro. Além disso, a estrutura do filtro permite trabalhar com um ganho consideravelmente menor ao trabalhar em ressonância, quando comparado a trabalhos anteriores. O sistema de controle foi testado no interferômetro de quadratura em malha aberta utilizando um interferômetro de realimentação virtual controlado, que dá equivalência da realimentação física. Este método de implementação foi escolhido devido à necessidade de maior taxa de amostragem e para evitar um maior atraso. O sistema proposto também foi estudado alterando a entrada do controlador (com e sem chaveamento, a estrutura da variável, e mudando a função de chaveamento de uma função de sinal para uma função sigmoide). Após o teste experimental, um atuador flextensional piezoelétrico foi avaliado sob todas as variações do sistema proposto, e então comparado sob a mesma medida ao método arco tangente clássico e a discrepância entre os métodos na faixa de 1.000 Hz foi menor que 5%, assim o sistema desenvolvido é validado para medições de fase óptica.



**Palavras-chave:** interferometria ótica; alto ganho; filtro ressonante; controle não linear.

# LIST OF FIGURES

# LIST OF SYMBOLS

| | |
|---|---|
| A | Factor of proportion [V] |
| $A_1$ | Coefficient matrix of the state variables regarding the input dynamics |
| $B_1$ | Coefficient matrix of the inputs regarding the input dynamics |
| $C_1$ | Coefficient matrix of the state variables regarding the output of the system |
| $C_2$ | Coefficient matrix of optical phase regarding the output of the system |
| $D_1$ | Coefficient matrix of the inputs regarding the output of the system |
| $E_0$ | Electric field of the laser source |
| $E_{01}$ | Amplitude of the electric field of the reference arm |
| $E_{02}$ | Amplitude of the electric field of the sensor arm |
| $E_R$ | Electric field of the reference arm |
| $E_S$ | Electric field of the sensor arm |
| $E_T$ | Electric field of the sensor arm |
| $G_{PZT_{fb}}$ | Feedback actuator gain [rad/V] |
| $G_{AMP}$ | Linear amplifier gain [V/V] |
| $G_{DC}$ | Gain of the filter in zero Hertz of frequency |
| $I_0$ | Optical intensity of the laser |
| $I_R$ | Optical intensity of the reference arm |
| $I_S$ | Optical intensity of the sensor arm |
| $K_0$ | Proportional gain (controller input without switching) |
| $K_1$ | Set of the stable equilibrium points |
| $K_2$ | Set of the instable equilibrium points |
| $T_s$ | Sampling period |
| $f_n$ | Resonant frequency [Hz] |
| $f_s$ | Sampling frequency [Hz] |
| $l_s$ | Total difference between the length of the arms in the absence of stimulus [m] |
| $n_s$ | Refraction index of the ambient |
| $v_{PD}$ | Voltage generated by the photodetector [V] |
| $v_{fb}$ | Feedback voltage [V] |
| $x_1$ | State variable |
| $x_2$ | State variable |
| $\omega_S$ | Modulation frequency [rad/s] |
| $\phi_0$ | Quasi-static phase between the arms [rad] |

| | |
|---|---|
| $\phi_c$ | Correction phase or controlling signal |
| $\phi_t$ | Total phase |
| $\Delta L$ | Displacement measured with the optical phase [m] |
| $\Delta\phi$ | Interest signal [rad] |
| $\in$ | Is an element of |
| $\mathcal{L}\{\cdot\}$ | Laplace transform |
| $\mathcal{L}^{-1}$ | Inverse Laplace transform |
| Q | Interferometer point of operation |
| $\mathbb{Z}$ | Set of integers |
| $\Gamma$ | Gain of the switching function (signal or sigmoidal function) of the controller |
| $A$ | Parameter of the gain filter ratio |
| $B$ | Parameter of the resonant filter transfer function for the discrete system |
| $C$ | Parameter of the resonant filter transfer function for the discrete system |
| $D$ | Parameter of the resonant filter transfer function for the discrete system |
| $G$ | Gain of the filter |
| $G(s)$ | Transfer function of the filter |
| $I$ | Irradiance, the optical intensity |
| $U(s)$ | Laplace transform of the input |
| $V$ | Visibility of the interference pattern |
| $a$ | Parameter of the resonant filter |
| $k$ | Constant of multiplicity |
| $s$ | Variable in frequency of the Laplace transform |
| $t$ | Time [s] |
| $u$ | Controller input |
| $v$ | Voltage generated by the photodetector normalized in AV factor [V] |
| $x$ | Phase modulation index [rad] |
| $y$ | Output of the system |
| $z$ | Variable of the z-plane |
| $\mathcal{Z}\{\cdot\}$ | Z-transform |
| $\lambda$ | wavelength of optical source radiation [nm] |
| $\pi$ | Number pi |
| $\omega$ | Optical frequency [rad/s] |
| $\omega$ | Optical frequency [rad/s] |

$\epsilon$ Sigmoid parameter of approximation

$\phi$ Total difference of phase between the arms or phase shift [rad]

# CONTENTS

# 1 INTRODUCTION

The interferometric principle is based on the interference of two light beams, usually laser beams, due the coherence that laser source offers, among others advantages. Using the interference phenomenon, the system works with the diffe405rence between the reference beam and the sensor one being able to measure whichever factor is disturbing the sensor, purposely. Its main purpose is to convert an optical phase variation between its arms in a variation of optical intensity, which can be measured electronically. This optical phase variation can be inserted in the system through many modes that it is possible to. In the case of this work it is inserted through an excited piezoelectric actuator that produces small displacements. The interferometric system has a high sensitivity, being able to measure mechanical displacements in the order of $10^{-14}$ m (YIMNIRUN *et al*, 2003). For this and others benefits, this system can be applied in many areas and for measurement of different physical quantities: nanotechnology (DEVASIA *et al*., 2007), samples' positioning in microelectronics (VERMA *et al*., 2005), masks' alignments and others sectors of fine mechanics, where there is need for microscopic positioning.

However, being so sensitive it has its disadvantages: the system can also capture environmental disturbances (such as vibrations, temperature variations, air turbulences, etc.). In other words, mitigate these effects it is one of the main challenges presented to interferometry. Thereby, due to the systems' nonlinear nature, problems as fading signal (SHEEM *et al*., 1982), as well as ambiguity of results and sense direction (CHEN *et al*.,2014) can appear and for that matter, making necessary the use of phase unwrapping algorithms (DEBNATH *et al*., 2009) which makes the measurement process complex, or else, the use of active compensations methods.

Over fifteen years now, the members of LOE - Laboratory of Optoelectronics (Faculty of Engineering of Ilha Solteira - FEIS, Universidade Estadual Paulista - UNESP), have been developing interferometry applications (MARTIN, 2018; MARTIN *et al*., 2017; GALETI *et al*., 2015a; GALETI *et al*., 2013; MARÇAL *et al*., 2012a; MARÇAL *et al*., 2012b; BARBOSA *et al*., 2010; MARÇAL *et al*., 2007), with special interest in the development of new techniques of detection of optical phase using low cost interferometers and simple electronic, and utilizing the advantages offered by the current digital signal acquisition and processing systems.

Due the challenges the interferometric system presents and in order to characterize new models of piezoelectric actuators, the members of LOE have been developing

unprecedented interferometric methods in the measurement of microscopic and submicroscopic displacements, processing the photodetected signals in the frequency (GALETI *et al*., 2015a; GALETI *et al*., 2013) or time domain (CONNELY, 2015; GALETI, *et al*., 2015b).

The temporal methods may require elements of active compensation (the interferometric system in closed loop) in order to operate around the quadrature condition (optimal point of operation) steadily in low gain mode (UDD; SPILLMAN, 2011), or, to linearize the interferometry characteristic curve, in high gain approach (CHEUNG *et al*., 2003), as proposed in this study.

This work comes to present a nonlinear control system with high gain approach for the two beam optical interferometer. The innovation brought here is to use the nonlinear control with a resonant filter. The goal is to explore the high gain approach without the need of interferometer in quadrature (FELÃO, 2019), which reduces the coast of extra optical elements. Once more the closed loop system operates with high gain approach, i.e. on full compensation, in order to linearize the interferometer transfer curve (not through the traditional Taylor series, but by closed loop control techniques) and eliminate a complex process of demodulation (which can involve phase unwrapping methods). Also, by using the resonant filter it is possible reduce the error of the system by using the resonant filter in resonance. This system ends up uniting two powerful tools of the nonlinear control: the resonant filter and a variable structure. The variable structure has been proved to be an important tool as well efficient and robust enough to stabilize the interferometer. Also, it is one of the main techniques of nonlinear control due to its simplicity of implementation and robustness characteristic (UTKIN, 1978; ITKIS, 1976; DECARLO *et al*., 1988).

Furthermore, its application to nonlinear systems, as in the case of the interferometric system, it strongly justified and allows satisfying the requirements of efficient operation of laser interferometers, guaranteeing high performance and robustness (MARTIN *et al*., 2017).

Chapter 2 presents a theoretical background regarding the two beam interferometer. It is described the Bulk Michelson interferometer (used in the experimental setups), the interferometer signal and its peculiarities. Also, the configuration of this interferometer in quadrature due an application proposed in Chapter 4.

The control theory is presented in Chapter 3: the controller proposed and its variations are described with the stability analysis along with its behavior. Also, they are tested preliminary via simulations in order to prove the theory described. Besides, a discrete analysis of the system had to be done due some issues regarding the sampling rate of the system.

Chapter 4 comes to present the experimental setup and the procedures used in tests presented in this research, as well as a brief description of the platforms used in the setups (hardware) and its connections. In the end of the chapter, a method of implementation is presented to solve some problems with the physical closing of the feedback control with the interferometric system.

All the results obtained are disclosed in Chapter 4 as well. The resonant control, those same problems of the modified control where predicted in Chapter 3. It was tested using the method of the virtual controller presented in Experimental Setup section of Chapter 4. The resonant control was tested for four different strategies in order to improve the gain relation far from the filter resonance and the chattering effect.

Finally, Chapter 5 brings the conclusions and discussion for future work.

# 2 TWO BEAM OPTICAL INTERFEROMETRY

Based on the experiment of Young (SALEH; TEICH, 2007; HARIHARAN, 2007), interferometers are optical devices based on the analysis of the interference pattern, which occurs by the superposition of two light beams: one took as the reference arm and the other being the sensor arm. This superposition causes a light pattern with maximums and minimums, where the sum or difference between the optical intensity of the beams had occurred, respectively. This distribution of intensity is named as fringe pattern.

Then, when any perturbation or stimulus is applied to the sensor arm, a displacement happens along the fringe pattern that can be measured and associated to the optical phase variation between the arms. This makes it possible the detection of minimum variations of optical phases (of the order of $10^{-8}$ rad) since the laser wavelength is small (of the order of micrometers). Therefore, it is possible to detect physical quantities with high sensitivity (LEÃO, 2004). In addition, the invention and developing of the laser in the 60's boosted the optical field during the $20^{th}$ century, especially the interferometry researches, thanks to the high level of temporal and spatial coherences that the laser provides.

Figure 1 – Bulk Michelson Interferometer.

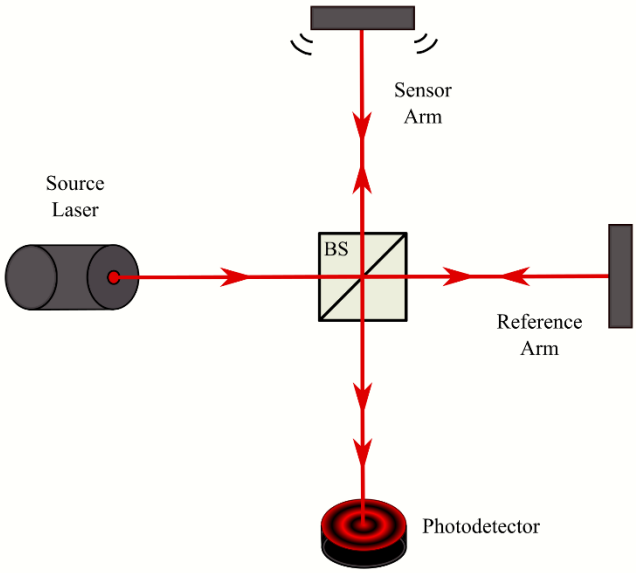


Source: from the author.

In the Figure 1 the bulk Michelson interferometer is presented: a two beam interferometer used mainly to measure sub micrometric displacements. As the setup in the figure shows, the neutral beam-splitter divides the laser beam coming from the source, with a 50/50 ratio, reflecting a beam to the sensor arm and transmitting the other beam to the reference arm. The beam in the sensor arm reflects back by a mirror attached to a actuator: the movement of the excited PZT and, consequently, the movement of the actuator insert a variation on the optical phase of the laser beam. With the information of the displacement of the actuator on the light phase, the beam reflected back by the mirror on the actuator is transmitted through the beam-splitter to the detector. The beam in the reference arm is reflected back by a fixed mirror and it is also reflected by the beam-splitter to the detector, superposing with the sensor beam and generating the fringe pattern on the photodetector (that transforms the intensity of light into an electrical signal).

In this case the pattern is circular, as shown the Figure 1, being the light intensity captured by the photodetector for analysis and signal processing. It is important to highlight that when the mirror bonded to the actuator moves, the interference pattern suffers a radial displacement according to the displacement direction $\Delta L(t)$. The complete displacement of a pattern corresponds to the mirror movement of $\lambda/2$, being the light wavelength in vacuum. In this case, for the Helium-Neon laser, $\lambda = 632{,}8\, nm$.

In other words, the pattern movement depends on the relative movement between the arms. So, it is important that the fixed mirror in the reference arm is static relative to the mirror on the actuator (sensor arm).

Due to the extremely sensitivity of the system, any spurious disturbance in the surroundings (such as mechanical noises and temperature variations) generates a random variation in the optical phase affecting the interferometric signal (output voltage of the photodetector) and causing signal fading. This consequence can be minimized by some stabilizing methods: the conditioning of the experiment surroundings (seismic isolation, for example, that raises the project costs); methods of automatic stabilization or passive compensation, which require techniques of signal processing. In this study it is preferable to reduce the signal fading by using control techniques.

## 2.1 THE INTERFEROMETRIC SIGNAL

The bulk Michelson interferometer presented in Figure 1 is considered homodyne, once the optical paths are at the same frequency. Besides, it is noteworthy that the neutral beam splitter does not create difference in the polarization of the beams. Likewise, that the laser

source has a high level of temporal and spatial coherences, being modeled as a monochromatic light source with harmonic temporal dependence. Bringing these to account, let's explore the equation of the interferometric system using fasorial notation.

An electric field $E_R(t)$ with amplitude $E_{01}$ is associated to the reference arm according to (1-a), and $E_S(t)$ with amplitude $E_{02}$ to the sensor arm according to (1-b). The total field $E_T$ is given by:

$$E_R(t) = E_{01}\ e^{j(\omega t)}, \quad (1-a)$$

$$E_S(t) = E_{02}\ e^{j(\omega t+\phi(t))}, \quad (1-b)$$

$$E_T = E_R(t) + E_S(t), \quad (2)$$

where $\omega$ is the optical frequency and $\phi(t)$ is the total difference of phase between the arms.

The photodetector used here obeys a quadratic law, which generates an electrical current/voltage directly proportional to the incident optical intensity. It can be described as the irradiance $I(t)$:

$$I(t) = \frac{E_T . E_T^*}{2}, \quad (3)$$

where $E_T . E_T^*$ is the product between the total field and its conjugate complex.

In accordance with Leão (2004) the optical intensity expression is given by:

$$I(t) = \frac{I_0}{2}\left[1 + V\cos\left(\phi(t)\right)\right], \quad (4)$$

where $I_0 = E_o^2/2$ is the optical intensity of the laser, regarding $E_{01} = E_{02} = E_0/\sqrt{2}$ . Because the beam-splitter has a 50/50 ratio, it is possible to declare that the optical powers in each arm are equals. The factor $V$ is the visibility of the interference pattern, being a measure of contrast between maximums and minimums values of $I(t)$.

The visibility is described by:

$$V = \frac{\sqrt{I_R I_S}}{\frac{I_R + I_S}{2}}, \quad (5)$$

with $I_R = I_S = \frac{E_{01}^2}{2}$ being the individual optical intensity of the reference arm and the sensor arm, respectively.

In doing so, the visibility assumes unitary value. In practice, it can assume values between 0 and 1($0 \leq V \leq 1$), due its dependency with the level of coherence of the optical source used, with the level of alignment and relative polarization (parallelism and

superposition) between the beams in the interferometer output. Thus, the ideal case ($V = 1$) is difficult to be stablished in practical ways, yet it is possible to obtain approximated values through precise alignment adjusts between the optical rays in the interferometric setup.

The phase shift $\phi(t)$ is given by the sum of the relative phase variation between the arms $\Delta\phi(t)$ and the static phase between the arms $\phi_0$:

$$\phi(t) = \Delta\phi(t) + \phi_0, \tag{6}$$

where $\Delta\phi(t)$ is the interest signal, induced by the stimulus which its desired to be measured.

Also, the different lengths of the interferometer arms, in the absence of signal, leads to the following expression for $\phi_0$ (Marçal, 2008):

$$\phi_0 = \frac{2\pi}{\lambda} n_s l_s, \tag{7}$$

where $\lambda$ is the wavelength of optical source radiation (in this case, $\lambda = 632{,}8\, nm$ for the He-Ne laser), $n_s$ is the refraction index of the ambient ($n_s = 1$ for air) and $l_s$ is the total difference between the length of the arms in the absence of stimulus.

In this study, the signal applied to the PZT is always sinusoidal and assuming linearity of the actuator, the sensor arm vibrates in the same way, thus:

$$\Delta\phi(t) = x\, sin(\omega_S t), \tag{8}$$

where $x$ is the phase modulation index (in radians) and $\omega_S$ is the modulation frequency.

At last, the signal voltage generated by the photodetector is described by (Marçal, 2008):

$$v_{PD}(t) = \mathrm{A}[1 + V\cos(\Delta\phi(t) + \phi_0)], \tag{9}$$

where A is an offset voltage regarding the optical intensity at the interferometer output, which contains information about the optical power of the laser source, the photodetector responsivity, the linear amplifier gain, among others.

Beyond the difficulty of precision alignment of the optical system, a challenge faced in measurements using the interferometer occurs mainly due environmental factors. When there are mechanical vibrations of low frequencies, thermal variation and air turbulences captured from the ambient nearby, it may appears a variation on the $\phi_0$ value in time (unpredictably) damaging the detected signal. The undesirable oscillation causes random variations of $\phi_0$ on the output signal $I(t)$ is known as fading problem of the photodetected signal $v(t)$. Since this variation happens slowly, $\phi_0$ is treated as $\phi_0(t)$, a quasi-static phase (MARTIN *et al.*, 2017).

## 2.2 SIGNAL FADING

For the various sources of $\phi_0(t)$, the analysis of the interferometer output signal (9) deserves a more detailed description. In (6), the variations in $\phi_0(t)$ imply a variation in the total phase $\phi(t)$, which impairs the interferometer output signal (9). In order to illustrate the phenomena of fading, it follows Figure 2.

Figure 2 – Optical transference curve of an interferometer.

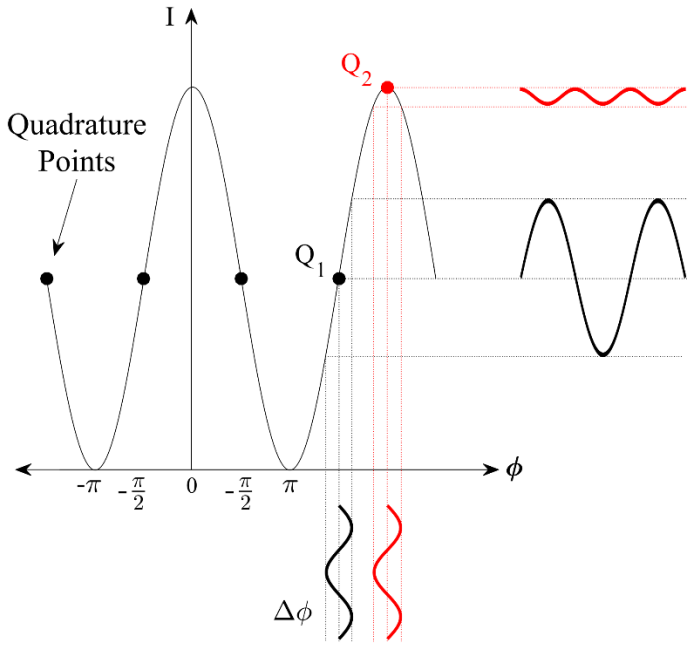


Source: from the author.

The curve in Figure 2 refers to (4), varying $\phi$ between $-\frac{3\pi}{2}$ and $\frac{5\pi}{2}\ rad$ and normalizing it with $I_0$ . The point $Q_1$ refers to a linear region or any point where $\phi_0$ is multiple odd of $\frac{\pi}{2}rad$. This way, the output signal is proportional to the input signal when operating over this quiescent point called quadrature condition (the optimal point of operation). Assuming (8), i.e., $\Delta\phi = x\sin(\omega_S t)$, under a low modulation index (where $x \ll \pi/2\ rad$) and quadrature condition ($\phi_0 = \pi/2\ rad$) with maximum visibility $V = 1$ in (4), it is obtained:

$$\frac{I(t)}{I_0} = \frac{1}{2}[1 + \cos(x\ sin\ \omega_S t + \pi/2)] \tag{10}$$

By developing the cosine by sum of arcs, and considering $x \ll \pi/2\ rad$ (using the following approximations: $sin(a) \cong a$ and $cos(a) \cong 1$ for $a << 1$), the equation can be rewritten as:

$$\frac{I(t)}{I_0} \cong \frac{1}{2}[1 - x\ sin\ (\omega_S t)] \tag{11}$$

Thus, the second portion on the right side of this last equation is proportional to $\Delta\phi(t)$ (given by (8)), disregarding the algebraic sign. Therefore, the second portion on the right side of (11) is a replica of the input signal $\Delta\phi(t)$ in accordance with Figure 2. For that, it is worth mentioning that the input signal could be an arbitrary waveform, since it has amplitudes lower then $\frac{\pi}{2} rad$ (low modulation depth).

A serious drawback in interferometry is that $\phi_0$ random variation can cause a distortion on the output signal in relation to the input one, in other words, the Q point can go from $Q_1$ to $Q_2$, as presented in the Figure 2, generating a distorted output signal with high second harmonic content. For that matter, if $\phi_0$ varies in a random way it can difficult the demodulation process.

For situations with high modulation index, where $x \gg \pi / 2\, rad$, the output signal is no longer proportional to the induced phase change $\Delta\phi\ (t)$ (which would be proportional to the input signal) even for quadrature condition of phase ($\phi_0 = \pi / 2\, rad$).This happens because the input signal amplitude goes through several periods of the cosine function in (4), causing a multi-fringe shift in the output signal, as shown in Figure 3.

Figure 3 – Transference curve of the optical intensity to signal with amplitude $x \gg \pi/2\ rad$, input and output.

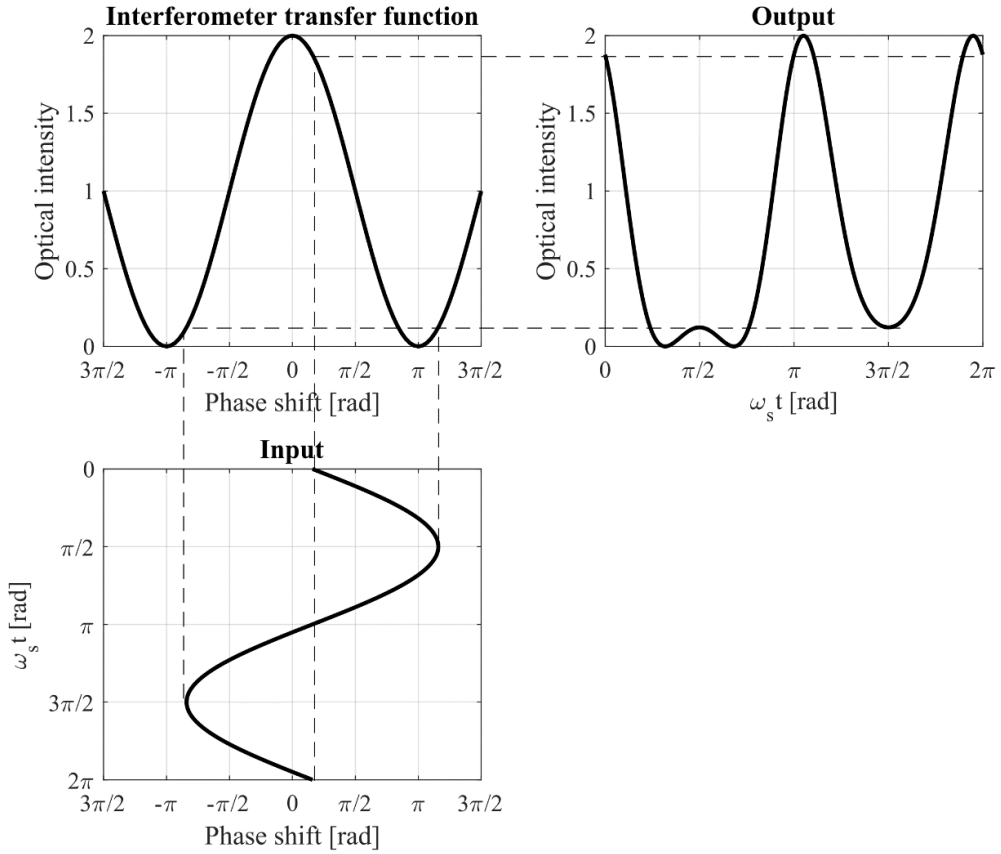


Source: modified from (MENEZES, 2009).

Figure 3 enables us to understand the nonlinear characteristic of the interferometer. The black curve is the characteristic curve at the interferometer, the red one is the input signal (the desired phase) and the blue one is the output signal (photodetected) under quadrature condition. As seen, the photodetected signal shows what is called multi-fringe mode (or turn around points, i.e. local maximum and minimum) which need a more complex demodulation method, called phase unwrapping.

Changing $\phi_0$ from $\pi\ /\ 2\ rad$ to some another value, the blue curve changes its shape drastically, even if the phase $\Delta\phi(t)$ remains unchanged. For practical interferometers, operating in open loop and under regular conditions of a non-metrological laboratory (no seismic isolation), the phase $\phi_0$ can vary dozens of radians in a few time. Therefore, if the interest is to measure values of $\Delta\phi(t) \ll 1\ rad$, the challenge of signal processing in interferometric systems is clearly noticed.

The fact that optical interferometry is an extremely sensitive sensor is the cause of the appearance of such phenomena (fading), not because of inefficiency: a paradox that can be

solved using signal processing techniques and automatic control, allowing us to benefit from all the advantages of the interferometer.

That is, as the smallest perturbations can distort the photodetected signal, instead of investing in a severe conditioning of the surrounding environment, optical phase detection methods are proposed that will be discussed later, in order to mitigate such disturbances.

## 2.3 THE QUADRATURE INTERFEROMETER

Among several configurations used to obtain the quadrature interferometer we have the one proposed in (Lemes, 2014), where an additional beam splitter is used to divide the output optical beam in two, to the photodetectors (PD1 and PD2): one set in the center of the fringe pattern and the other slightly displaced to achieve quadrature, such as Figure 4.

The position of the second photodetector can be adjusted based on the Lissajous figures for an elliptical form not inclined, using an oscilloscope on the XY mode and the photodetected signals on channels 1 and 2.

Figure 4 – The quadrature experimental setup diagram.

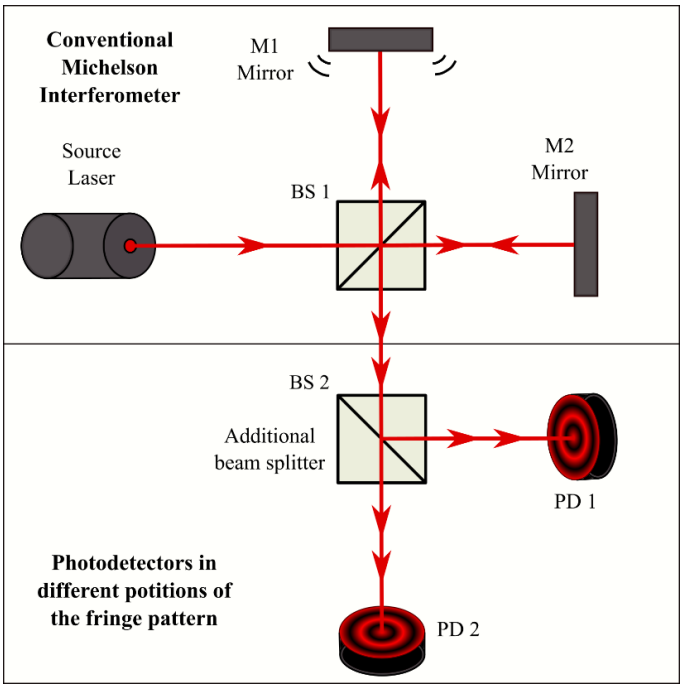


Source: from the author.

## 2.4 ACTIVE HOMODYNE DEMODULATION OF INTERFEROMETRIC SIGNAL WITH NONLINEAR CONTROL

Due the nature of this work, this section is about the two approaches that literature present us for active homodyne demodulation: the low gain and the high gain approach (UDD; SPILLMAN, 2011).

### 2.4.1 Low gain approach

The low gain approach compensates only $\phi_0$ the environmental disturbance, which is a low frequency signal, so the gain of the control system does need to be as great as in the high gain approach. Besides compensating the disturbance, it also has to maintain the system on quadrature position (Martin, 2018), then:

$$\phi = \Delta\phi(t) + \phi_0 - \phi_c = \Delta\phi(t) + \pi/2, \tag{12}$$

where $\phi_c$ is the controlling signal.

According to Galeti (2011), from equation (9), we can write the time-varying component of the quadrature output interferometric signal as:

$$v(t) \cong - AV\ sin\Delta\phi(t) \tag{13}$$

### 2.4.2 High gain approach

The high gain approach receives this name because the gain of the control system has to be high enough to compensate both $\Delta\phi(t)$ and $\phi_0$, while trying to maintain the system on quadrature position (Martin, 2018), thus:

$$\phi = \Delta\phi(t) + \phi_0 - \phi_c = \pi/2 \tag{14}$$

where $\phi_c$ is the controlling signal.

Because the controlling system compensates both signals, the time-varying interferometer output $v(t)$ from (4) stays in zero position and works at quadrature condition as the previous equation points out. So, the controlling signal is directly proportional to the feedback voltage $v_{fb}$ which contains the interest signal (Martin, 2018), being that:

$$\phi_c = G_{AMP}.G_{PZT_{fb}}.v_{fb} \tag{15}$$

where $G_{AMP}$ is the linear amplifier gain in $[V/V]$ used to drive the actuator in the feedback loop with the controlling signal, and $G_{PZT_{fb}}$ is the gain of the feedback actuator. For this to

work out $G_{PZT_{fb}}$ needs to be well defined being the reason for its previous characterization as described previously.

This is one of the biggest advantages of this approach: no additional demodulation method is needed once it converts the transfer curve of the interferometer to a straight line enabling us to work with both modulation indexes, low and high, because it has a much higher range for amplitude, regarding that feedback actuator also operates on it liner region (MARTIN, 2018). To guarantee quality for measurements above 20 Hz a filtering process is required as in (UDD; SIPILLMAN, 2011) to separate the interest signal from the disturbance signal.

The system to be presented in this research works with high gain approach, but thanks to its realization, the gain does not need to be as greater as the previous techniques (Martin, 2017; Felão, 2018).

# 3 NONLINEAR CONTROL SYSTEM BASED ON VARIABLE STRUCTURE AND SLIDING MODES

This chapter briefs the theory researched and developed throughout this work. The main idea is developing a control system that needs only one interferometric output voltage, operates with high gain approach, gathering the resonant filter and a variable structure. The system under study unfolds in four analog systems (variations). For all systems proposed, we present the control law, stability studies, simulations and their particular characteristics.

Throughout this work, the main strategy is to use variable structure and sliding modes within the control systems. Already proved to be powerful for controlling interferometric systems (Martin et. al, 2017; Felão et. al, 2019), and it not only stabilizes the plant but also eases the data processing. Evermore, it brings great advantages, such as low sensitivity to plant parameters variations and disturbances, eliminating the necessity of exact modeling, thereby reducing the complexity of the feedback control design (DeCarlo *et al.*, 1988; Utkin, 1978). The application of such technique in a nonlinear plant as the interferometer is conceivable and has simplicity of implementation and robustness (Martin et. al, 2017; Felão et. al, 2019). Within these advantages, we propose to combine the variable structure with a resonant filter, hoping we can work in its resonance in order to reduce the total gain of the controller, since the system operates with high gain approach. More will be shown ahead.

## 3.2 THE RESONANT FILTER

The first idea was to combine two powerful tools: a resonant filter and a variable structure. As seen in previous works (MARTIN *et al*., 2017; FELÃO, 2018) variable structure and sliding modes (DECARLO *et al*., 1988) (UTKIN, 1978) have been proved to be a powerful strategy in order to control and stabilize a two beam optical interferometer, providing robustness to the system. And the resonant filter seems to have some interest behavior in such system. In linear control, when we add to the open loop transfer function a resonant filter, then if the controlled is stable, it can be shown that the error between the plant output and a sinusoidal reference signal with the same frequency of the resonant filter, will be equal to zero. It means that one obtains a tracking condition. We can begin by analyzing the behavior of the resonant filter in the closed loop within the interferometric system and then combine them.

In Figure 5, the block diagram of the feedback system proposed for the stabilization of the interferometer is presented. This is a second-order system due to the resonant filter. The

'interferometer' block is (9) with suppression of the voltage bias (A), being possible by using a DC suppressor block within the control implementation.

Figure 5 – Block diagram with the general control proposal.

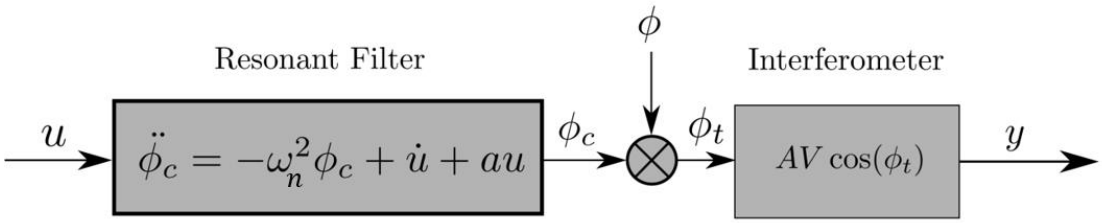


Source: from the author.

From Figure 5, it can be concluded that

$$y = AVcos(\phi_c + \phi) = AVcos(\phi_t), \tag{16}$$

where $y$ is the output signal. According to (6), the phase shift is given by:

$$\phi = \Delta\phi + \phi_0, \tag{17}$$

where $\phi$ is the total optical phase, composed by $\Delta\phi$, the interest signal, and $\phi_0$, an environmental disturbance of low frequency (usually below 20 Hz). The phase $\phi_c$ is the correction signal. The parameter '$AV$' is always positive and comes from physical set up of the interferometer.

The input signal ($u$) of the system can be given by (18) or (19), as will be seen ahead:

$$u = -\Gamma\, sgn(y), \tag{18}$$

$$u = -\mathrm{K_0 y} \tag{19}$$

where $sgn(-)$ is the sign function related with the switching control action. The controller gain is '$\Gamma$' or '$K_0$', both positive. When (19) is chosen, the resonant filter is allied to a gain only, and when we choose (18), the control has variable structure and can present sliding modes.

For first impressions on how the filter works, one can analyze its equation. The 'Resonant Filter' block describes the differential equation of the filter that can be written as:

$$\ddot{\phi}_c(t) + {\omega_n}^2 \phi_c(t) = \dot{u}(t) + au(t), \tag{20}$$

where $\omega_n$ is the resonance frequency in [rad/s] and $a$ is a parameter of the resonant filter that we often define as $a = {\omega_n}^2$ for unitary low frequency gain of the resonant filter, as will be shown furthermore.

Applying Laplace transform $\mathcal{L}\{\cdot\}$ to (20) and considering as initial conditions $\phi_c(0^-)$, $\dot{\phi}_c(0^-)$ and for either input is considered $u(t) = \dot{u}(t) = 0$ for $t < 0$, it can be obtained:

$$s^2\phi_c(s) - s\phi_c(0^-) - \dot{\phi}_c(0^-) + {\omega_n}^2\phi_c(s) = sU(s) + aU(s). \tag{21}$$

This can be rewritten as:

$$\phi_c(s) = \frac{s\phi_c(0^-) + \dot{\phi}_c(0^-)}{s^2 + {\omega_n}^2} + \frac{s+a}{s^2 + {\omega_n}^2}\ U(s). \tag{22}$$

First, disregarding $\phi_0$ and considering $\phi = \Delta\phi = x\ sin(\omega_n t)$, if $\phi_c(0^-) = 0$ and $\dot{\phi}_c(0^-) = x\omega_n$, then:

$$\phi_c(s) = \frac{x\omega_n}{s^2 + {\omega_n}^2} + \frac{s+a}{s^2 + {\omega_n}^2}\ U(s). \tag{23}$$

We can observe that the Inverse Laplace transform $\mathcal{L}^{-1}\{\cdot\}$ of the first term from (23) is given by $\mathcal{L}^{-1}\left\{\frac{x\omega_n}{s^2 + {\omega_n}^2}\right\} = x\ sin(\omega_n t)$. Thereby, the interest signal $\Delta\phi$ can be generated by an initial condition of the controller. In other words, it is possible to use this structure to produce a correction signal ($\phi_c$) to stabilize the interferometer on its optimal point of operation. The main idea is to consider the signal $\phi = x\ sin(\omega_n\ t)$ as a signal obtained in the output of the resonant filter (20)-(23), for suitable initial conditions $\phi_c(0^-)$ and $\dot{\phi}_c(0^-)$. This fact helps the analysis of the controlled system given in Figure 5 with the control law (18) or (19), because in this case it is not necessary to represent $\phi = x\ sin(\omega_n\ t)$ as an external signal, that is not related with the system equations. This is a preliminary analysis disregarding the disturbance ($\phi_0 = 0$), the case where $\phi_0 \neq 0$ will be seen ahead within the cases simulations.

### 3.2.1 System modeling

Since the system seems to be promising, we can model it by conveniently choosing the state variables ($x_1,\ x_2$). So, (20) can be expressed as:

$$\ddot{\phi}_c(t) = \dot{u}(t) + au(t) - {\omega_n}^2\phi_c(t) = \dot{u} + \dot{x}_2, \tag{24}$$

such that

$$\begin{cases} x_1 = \phi_c \\ \dot{x}_1 = \dot{\phi}_c = u + x_2 \\ \dot{x}_2 = au - {\omega_n}^2 x_1 . \end{cases} \tag{25}$$

Then, the block diagram can be redrawn as in Figure 6.

Figure 6 – Modified block diagram with state variables.

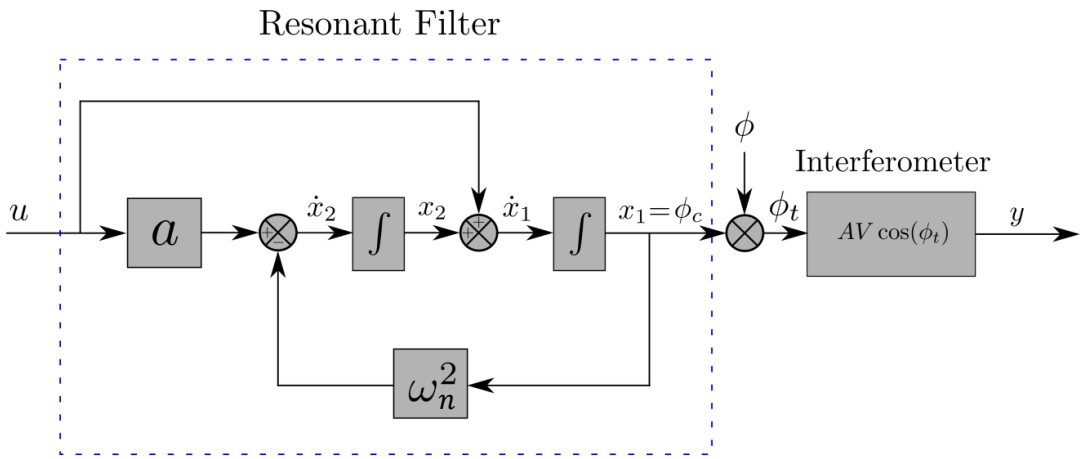


Source: from the author.

Once the output is:

$$y = AVcos(x_1 + \phi) = AVcos(\phi_t), \tag{26}$$

it can be rewritten as:

$$y = \frac{(x_1 + \phi + \pi/2)}{(x_1 + \phi + \pi/2)} AVsin(x_1 + \phi + \pi/2). \tag{27}$$

This way, (25) and (27) can be written in matrix form, and the system can be expressed as:

$$\begin{cases} \dot{x} = A_1 x + B_1 u \\ y = C_1 x + D_1 u + C_2(\phi + \frac{\pi}{2}), \end{cases} \tag{28}$$

where $x = \begin{pmatrix} x_1 \\ x_2 \end{pmatrix}$, $\dot{x} = \begin{pmatrix} \dot{x_1} \\ \dot{x_2} \end{pmatrix}$ and

$$A_1 = \begin{pmatrix} 0 & 1 \\ -\omega_n{}^2 & 0 \end{pmatrix}, \; B_1 = \begin{pmatrix} 1 \\ a \end{pmatrix} \tag{29}$$

$$C_1 = \begin{pmatrix} \frac{AVsin(x_1 + \phi + \pi/2)}{(x_1 + \phi + \pi/2)} & 0 \end{pmatrix}, D_1 = 0, C_2 = \begin{pmatrix} \frac{AVsin(x_1 + \phi + \pi/2)}{(x_1 + \phi + \pi/2)} \end{pmatrix} \tag{30}$$

Given (29) and (30), then the proposed structure of the resonant filter seems to be adequate to design controllers for the interferometer, based on Takagi-Sugeno fuzzy models.

### 3.2.2 Sliding surface

For the input (18), the system presents switching, therefore has variable structure and may present sliding modes. Accordingly, we can define the sliding surface (Utkin, 1978) and its conditions, in order to obtain the equations of phase correction signal $\phi_c$. This method is used to obtain the control signal of a continuous dynamic system equivalent to the original discontinuous one, considering that the system is confined in the slide surface, by imposing $s = 0$ and $\dot{s} = 0$, where s depends on the state vector of the plant and is specified in the design. A suitable choice (Felão, 2019) for the sliding variable comes from (26):

$$s = y = AVcos(x_1 + \phi) = AVsin(x_1 + \phi + \pi/2), \tag{31}$$

then

$$\dot{s} = \dot{y} = AV\left(\dot{x}_1 + \dot{\phi}\right) cos(x_1 + \phi + \pi/2). \tag{32}$$

As the first condition is $s = 0$ for (31), for that matter:

$$x_1 + \phi + \pi/2 = k\pi, \;\; k \in \mathbb{Z}, \tag{33}$$

where Z = {..., -2, -1, 0, 1, 2, ...}. Thereby, the system has infinite points of equilibrium (P.E.). Their stability will be investigated in the next section.

By the other hand, for $\dot{s} = 0$ on (32), one can observe that applying (33) the cosine function obeys $cos(x_1 + \phi + \pi/2) = \pm 1$, and thus its different from zero, so $\dot{x}_1 + \dot{\phi} = 0$ or :

$$\dot{x}_1 = \phi_c = -\dot{\phi}. \tag{34}$$

Consequently, one can say that for the system confined into the sliding surface the correction signal ($x_1 = \phi_c$) follows the total phase ($\phi$).

Looking at (23) and Figure 14, the transfer function of the resonant filter disregarding its initial condition, is given by:

$$G(s) = \frac{\phi_c(s)}{U(s)} = \frac{s+a}{s^2+{\omega_n}^2} \ . \tag{35}$$

Therefore, for the system convenience it is adopted $a = {\omega_n}^2$. So, the gain in lower frequencies ($s \to 0$) is $G_{DC} = 1$, and the gain at the frequency of operation ($s \to \pm j\omega_n$) is $|G(s)| \to \infty$, as shown in the Bode diagram (Figure 7).

Figure 7 – Bode Diagram of the Resonant Filter for $\omega_n$= 200$\pi$ rad (or 100 Hz)

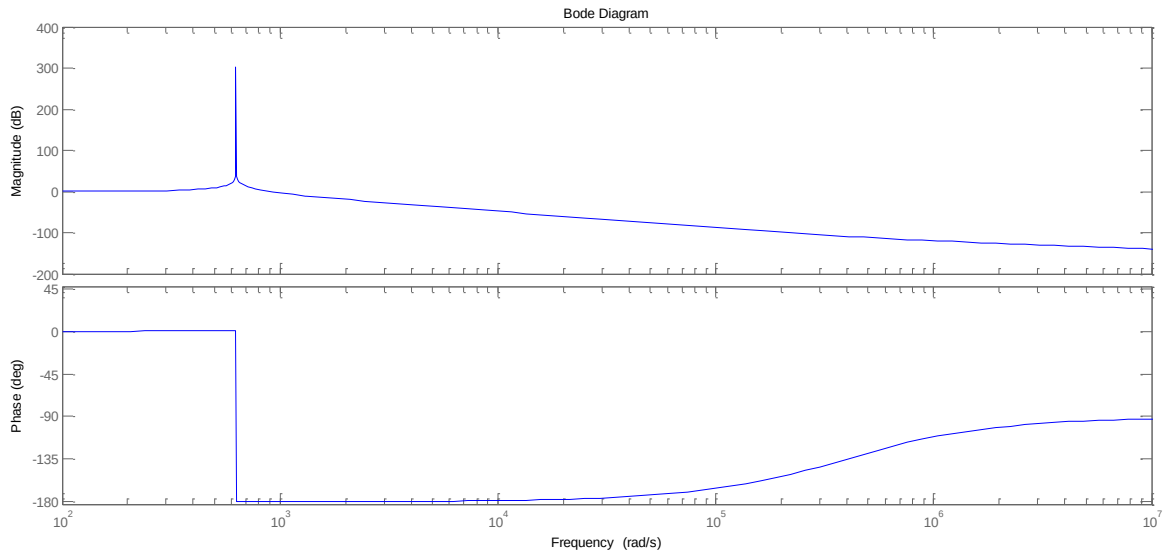


Source: from the author.

Therefore, if the system operates in the resonant frequency the gain of filter (G) goes to infinite and assuming the system is on the sliding surface, the gain of the controller (Γ as in (18)) should be minimum to control the system. As will be observed ahead, if the interest signal is at any frequency below the resonant frequency, the system can also compensate it, but at a greater gain (Γ). If the interest signal is at a frequency above the resonance frequency of the filter, the gain should be even greater due the attenuation in the magnitude of the filter (-40dB per decade of frequency), causing the chattering effect to be noticeable or even to take the system to instability.

For this matter, we can observe that the filter is able to compensate both interest sign '$\Delta\phi$' and environmental disturbance '$\phi_0$' even if both signals are at or under the resonance frequency, once the gain ($\Gamma$) is enough. Thence, the system operates in high gain approach (all the optical phase can be compensated). Also, since the resonant filter filters the resonant frequency, when its operating in the resonance (the frequency of the interest signal is the same of the resonant filter), the error of the system should be minimum, resulting in a smooth response, without the need of data processing, such as noise filter for example.

Also, looking at the magnitude spectrum, the filter behaves as a lock-in device, used to filter specific frequencies in order to measure really small displacements using the interferometer (Yimnirun et. al, 2003). This could be a future application of this controller, eliminating the need of such device in the process.

### 3.2.3 Stability

Due the system realization, we can analyze the stability of the equilibrium points by considering the switching control law (18) in the state space (25), thus:

$$\begin{cases} \dot{x}_1 = x_2 - \Gamma sgn(y) \\ \dot{x}_2 = -{\omega_n}^2 x_1 - a\Gamma sgn(y) \end{cases}, \tag{36}$$

where $y$ is given by (26) and we can replace it in the first equation of (36):

$$\dot{x}_1 = x_2 - \Gamma sgn(AVcos(\phi_t)) \text{ and } \phi_t = x_1 + \phi. \tag{37}$$

So, if $y > 0$ (since $AV > 0$ and considering $-\pi/2 < \phi_t < \pi/2$), (36) becomes $\dot{x}_1 = x_2 - \Gamma$. Therefore, note that from (36) and (37), $\dot{\phi}_t = \dot{x}_1 + \dot{\phi} = x_2 - \Gamma sgn\big(AVcos(\phi_t)\big) + \dot{\phi} = x_2 - \Gamma + \dot{\phi} \leq |x_2| - \Gamma + |\dot{\phi}|$. Then, if the gain '$\Gamma$' is greater enough ($\Gamma > |x_2| + |\dot{\phi}|$) it dominates the uncertainty and $\dot{\phi}_t < 0$, meaning that $\phi_t$ decays and it goes to $-\pi/2$. By the other hand, if $y < 0$ (for $-\frac{3\pi}{2} < \phi_t < -\pi/2$), (36) becomes $\dot{x}_1 = x_2 + \Gamma$ and $\dot{\phi}_t > 0$, meaning that $\phi_t$ increases and $\phi_t$ goes to $-\pi/2$. The graphic interpretation of this analysis is shown in Figure 8.

As analyzed before and shown in Figure 8, one can conclude that the equilibrium points can be classified as:

$$\text{Stable for } (\tfrac{\pi}{2} + k\pi) \text{ where } k \in K_1 = \{\dots, -3, -1, 1, 3, 5, \dots\}, \tag{38}$$

Instable for $(\frac{\pi}{2} + k\pi)$ where $k \in K_2 = \{\ldots, -2, 0, 2, 4, \ldots\}$. (39)

Figure 8 – Graphic interpretation: stability of the equilibrium points in the output characteristic curve of the interferometer.

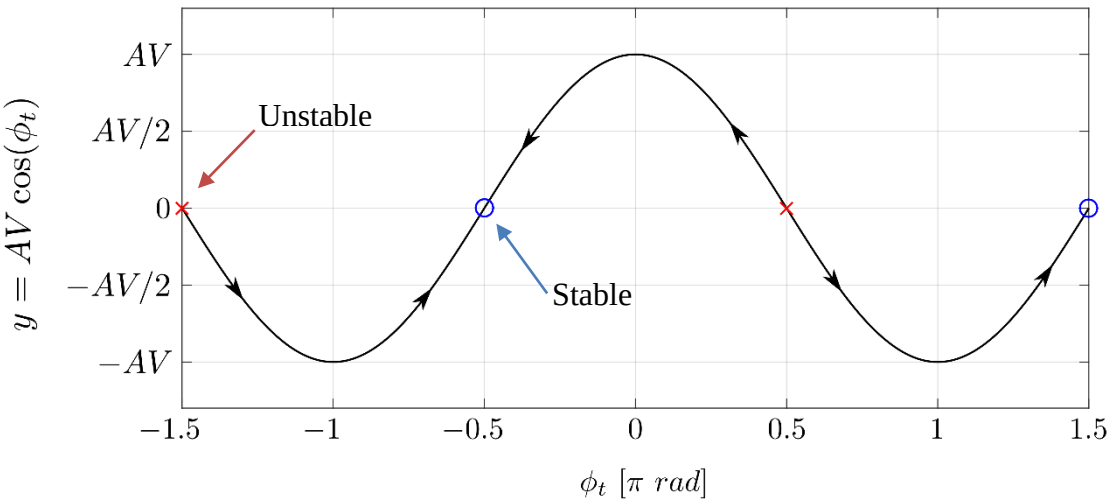


Source: from the author.

For the other input (19), the system has similar operation. But, since there is no switching, it goes to the closest equilibrium point and stays there even throughout disturbances. It will only change the equilibrium point, if restarted (once the initial conditions also change). In a way, the switching is what gives the system robustness (since it presents variable structure and also sliding modes), but it is an additional operation to the system too (regarding a digital implementation, for example). So, the system operating without switching loses robustness but works in less operations.

Analyzing the closed loop system for the (19) input, considering that $u = -y$ $(K_0 = 1)$. In that case the system in closed loop is stable and $y = 0$ in steady-state. Once the closed loop system is stable, we consider $y = AV\phi(t)$ and disregard the disturbance $(\phi_0 = 0)$. The system poles of the closed loop are given by:

$$1 + \frac{AV(s+{\omega_n}^2)}{s^2+a}, \text{ for } a = {\omega_n}^2, \tag{40}$$

$$s^2 + AVs + (AVa + a) = 0, \tag{41}$$

for $AV$ and $a$, positives. Then all the system's poles have negative real part, proving to be stable.

This second input (18) was proposed, when looking for a minimum gain of the system, resulting in a two alternative systems: one following the input (18), and combining (18) - (19):

$$u = -K_0 y - \Gamma sgn(y) \tag{42}$$

The main idea is that the component of (17) in (42) would dominate the uncertainty ($\phi_0$). For that matter, the gain $\Gamma > 0$ could be relatively small.

### 3.2.4 Simulations

In this section the simulations based on the closed loop of the control system are presented for all three systems discussed in this section. All these simulations were carried out by using the software *Simulink (Matlab)*. The tests were done for the continuous and the discrete systems.

#### *3.2.4.1 Continuous system's simulations*

The continuous system the resonant filter is simulated using its Laplace equation from (35), considering the switching (input from (18)). Figure 9 shows the control strategy used in closed loop topology, the same design was used in the simulations.

Figure 9 – Control strategy proposal: the resonant filter with switching.

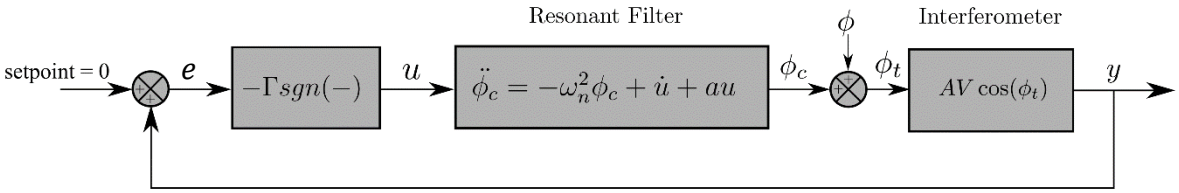


Source: from the author.

The block diagram used built in Simulink is shown in Figure 10, adopting $a = {\omega_n}^2$.

Figure 10 – Block diagram for the continuous simulation on Simulink, control system considering the switching ($u = -\Gamma sgn(y)$).

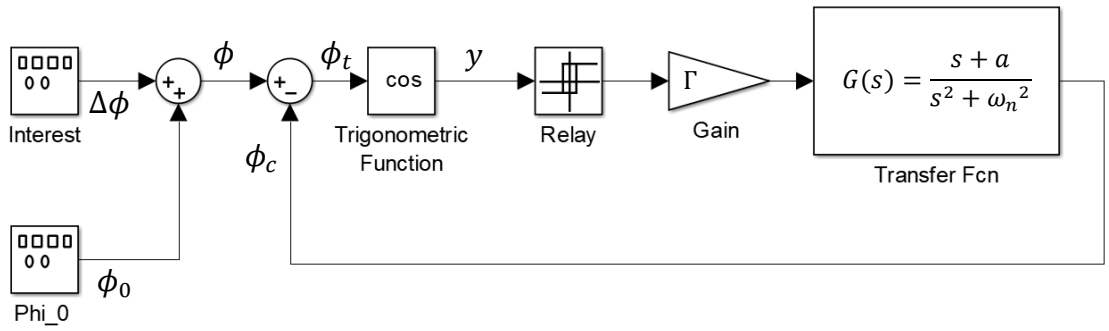


Source: from the author.

At first, the system was simulated disregarding the environmental disturbance (considering $\phi = \Delta\phi$, with $\phi_0 = 0$) and using a sinusoidal signal as the interest signal, shown in Figure 11. In the simulation, $\Delta\phi$ amplitude is 1V, $f_n = \frac{\omega_n}{2\pi} = 100$ Hz and $\Gamma = 100$ were used.

From Figure 11, one can observe that the correction signal follows the interest signal as expected. Also, it conducts the corrected phase ($\phi_c$) to $-\pi/2$ and the interferometer signal goes to zero. From interferometric curve (in green) we observe a settling time of 0.02 s. This proves the affirmations made previously, accordingly (33) and (34).

Figure 11 – Closed loop control system disregarding $\phi_0$, for sinusoidal $\Delta\phi$ (interest signal) with 1 V of amplitude, 100 of frequency, and gain $\Gamma = 100$. Operating in resonance (filter's and signal frequency are the same). Also, the interferometric signal ($y$) and the correction signal ($\phi_c$).

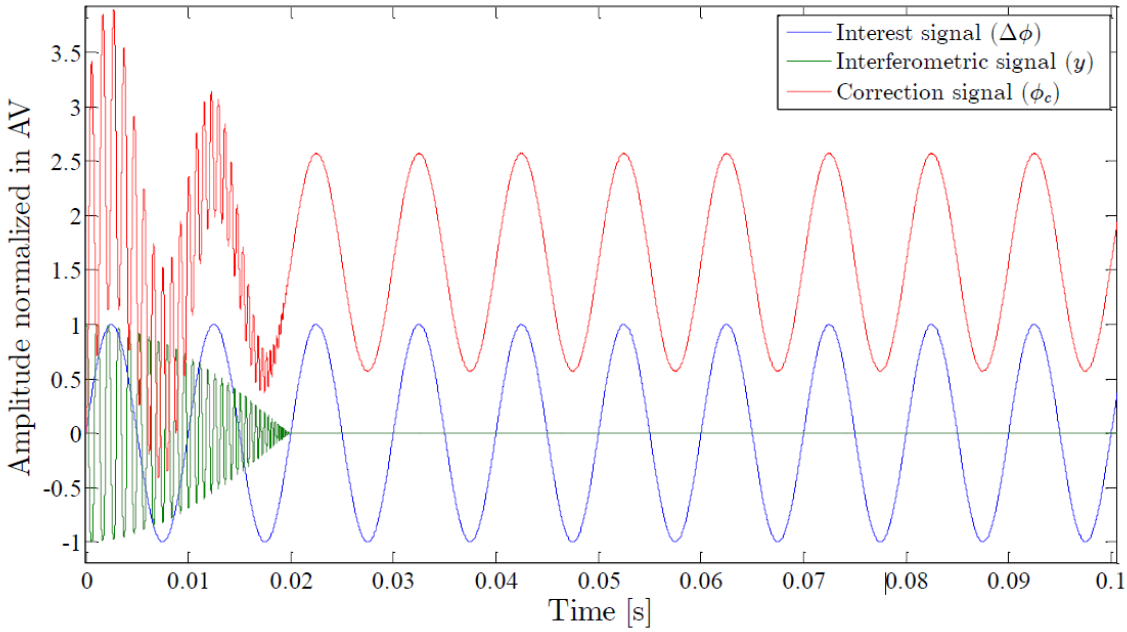


Source: from the author.

For the same conditions of $\Delta\phi$, the simulation was also carried out considering the presence of environmental disturbance, as in Figure 12, for sinusoidal $\Delta\phi$ amplitude = 1 V, 100 Hz of frequency ($f$), gain $\Gamma = 100$, $\phi_0$ sinusoidal with 2 V of amplitude and 5 Hz of frequency. Operating in resonance (filter's and signal frequency are the same, thereby $f = f_n = 100$ Hz)

Figure 12 – Closed loop control system considering $\phi_0$ sinusoidal with 2 V and 5 Hz, for $\Delta\phi$ (interest signal) sinusoidal with 1 V and 100 Hz, and gain $\Gamma = 200$. Operating in resonance (filter's and signal frequency are the same). Also, the interferometric signal ($y$), the correction signal ($\phi_c$) and the total phase ($\Delta\phi + \phi_0$).

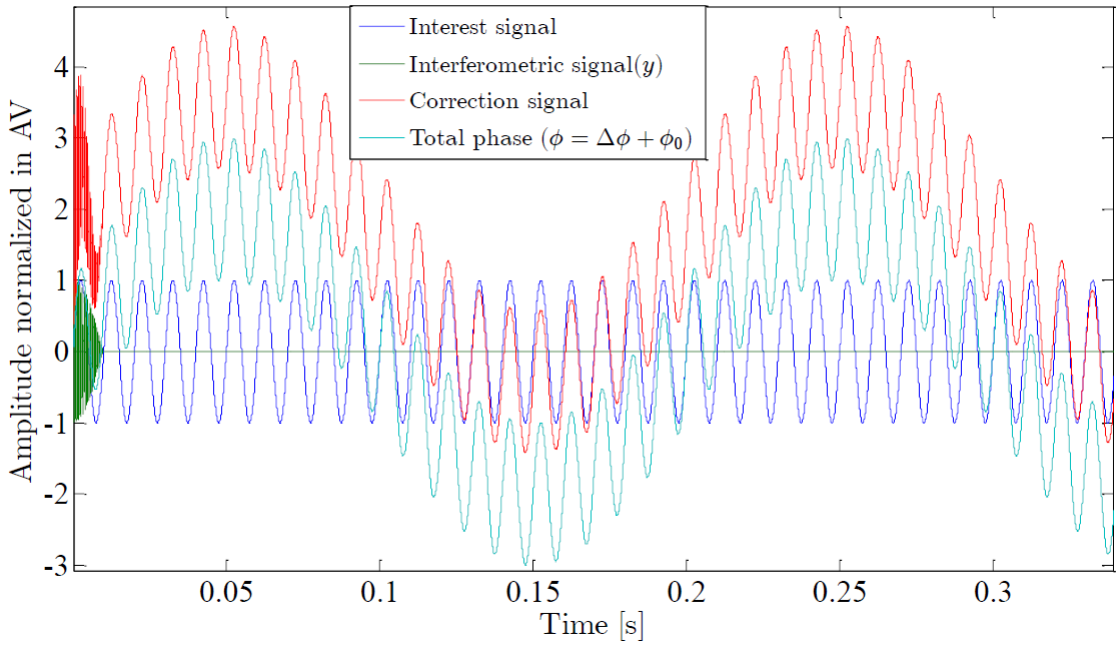


Source: from the author.

Figure 12 shows clearly that even with presence of the applied disturbance $\phi_0$ the system yet stabilizes: the correction signal follows the interest signal, and the corrected phase conducts the interferometric signal to the quadrature condition ($-\pi/2$). One can conclude that the interferometer operates under the high gain approach, according with (Udd & Spillman, 2011).

From Figure 11 we can also observe that the settling time (0.02 s) is slightly reduced when compared to Figure 12 (0.01 s). The difference relies in the gain (Γ): the greater the gain, the smaller the time of settling. Also, a fact that interferes is the filter parameter '$a$', which is a fixed parameter. In order to be able to choose a smaller gain, we could increase '$a$' currently adopted as $a = {\omega_n}^2$.

For the interest signal ($\Delta\phi$) at 100 Hz and 1 V peak, the tested gain was $\Gamma = 200$ (Figure 12). But, for the same conditions the minimum gain possible was $\Gamma = 4$ , Figure 13.

Figure 13 – Closed loop control system considering $\phi_0$ sinusoidal with 2 V and 5 $Hz$, for $\Delta\phi$ sinusoidal with 1 V and 100 Hz, and gain $\Gamma = 4$.

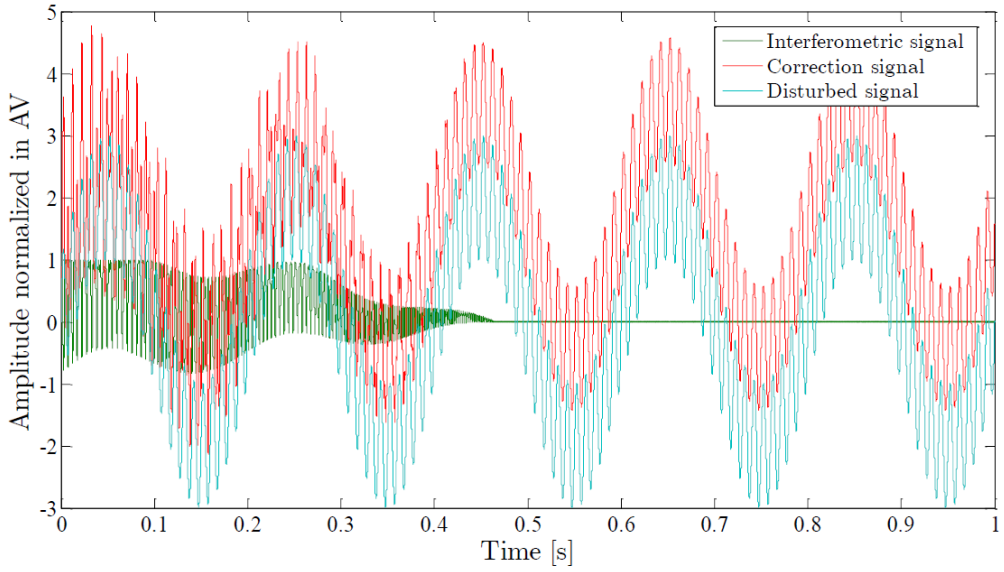


Source: from the author.

Using the gain $\Gamma = 4$, the Figure 13 shows settling time of 0.46 seconds. After that, the correction signal follows the total phase (assigned as 'disturbed signal'). Exaggerating the gain to $\Gamma = 1000$, the Figure 14 is obtained.

Figure 14 – Closed loop control system considering $\phi_0$ sinusoidal with 2 V and 5 Hz, for $\Delta\phi$ sinusoidal with 1 V and 100 Hz, and gain $\Gamma = 1000$.

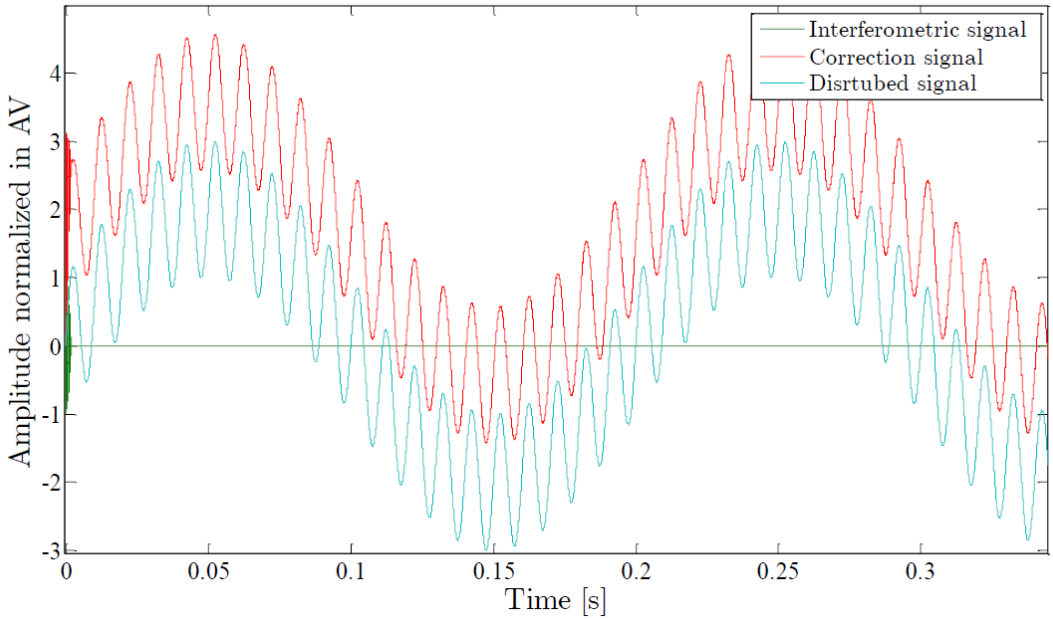


Source: from the author.

Figure 14 shows that for this adjusted gain ($\Gamma = 1000$), the settling time is reduced to 0.005 seconds. So, there is no need of a higher gain once the control works with a minimum gain ($\Gamma = 4$, in this case) and the acquisition can be done after the establishment.

Thereon, opening the loop in Figure 9 and 19 the system was simulated, as shown in Figure 15. The corresponding correction signal is shown in Figure 16.

Figure 15 - Open loop control system considering $\phi_0$ sinusoidal with 2 V and 5 Hz, for $\Delta\phi$ sinusoidal with 1 V and 100 Hz, showing the interferometric and the disturbed signal.

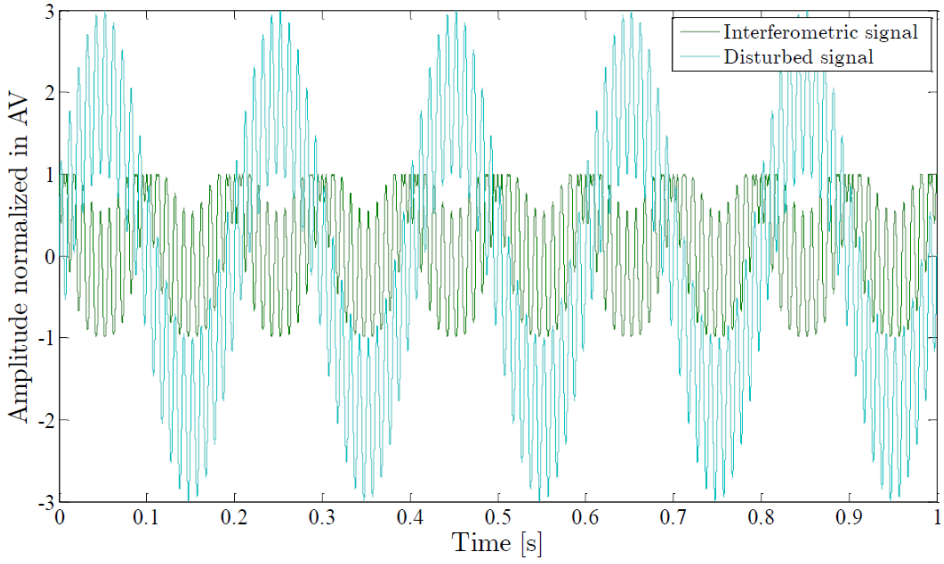


Source: from the author.

Figure 16 - The correction signal for the open loop control system considering $\phi_0$ sinusoidal with 2 V and 5 Hz, for $\Delta\phi$ sinusoidal with 1 V and 100 Hz.

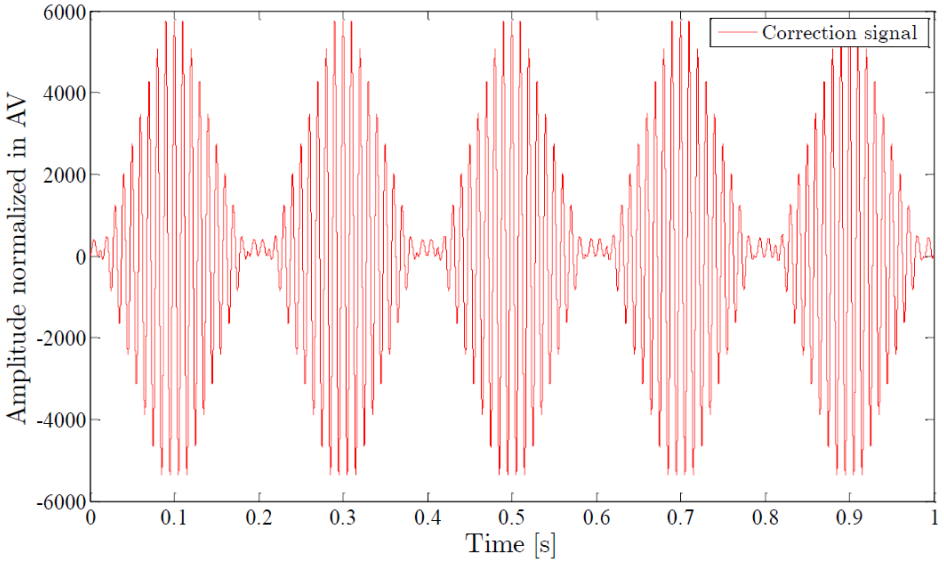


Source: from the author.

As expected, in Figure 15, the interferometric signal is not proportional to the correction signal neither to the total phase (assigned as ‘disturbed signal’). Also, in Figure 16, the correction signal does not converge (goes to zero), showing that in open loop the total phase is not compensated, nor is equal the correction signal.

Now, considering the input (19), the proportional input (system without switching), the control strategy proposed is shown in Figure 17.

Figure 17 – Control strategy proposal: the resonant filter without switching.

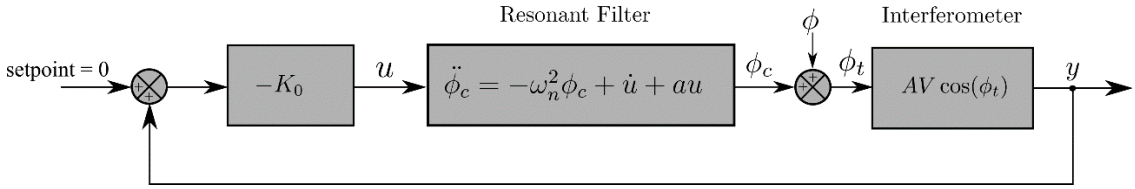


Source: from the author.

And the system simulated without switching is presented in Figure 18, considering $a = {\omega_n}^2$.

Figure 18 - Block diagram for the continuous simulation on Simulink, control system without the switching.

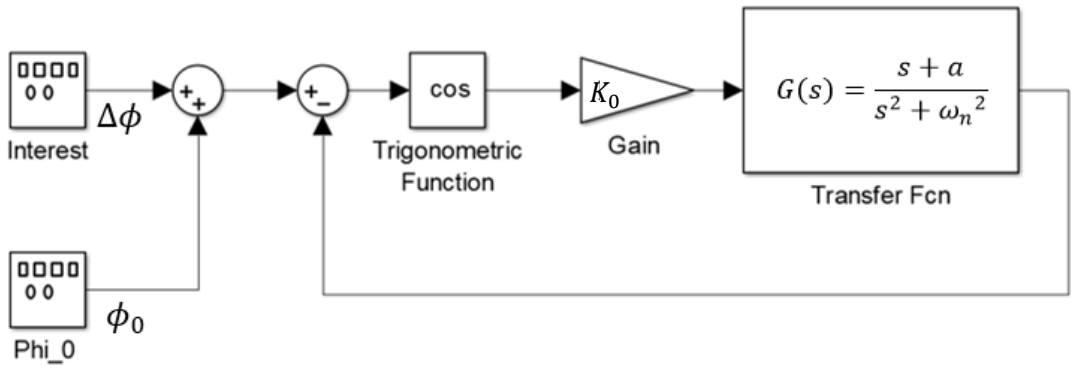


Source: from the author.

Following the simulation procedure of the control system with switching, first we disregard the environmental disturbance (considering $\phi = \Delta\phi$, with $\phi_0 = 0$) and use a sinusoidal signal as the interest signal, obtaining the result shown in Figure 19. In this simulation we use the following parameters: amplitude of $\Delta\phi$ equal to 1 V, $f_n = 100$ Hz and $\mathrm{K}_0 = 100$.

Figure 19 - Closed loop control system (without switching) disregarding $\phi_0$, for sinusoidal $\Delta\phi$ (interest signal) with 1 V of amplitude, 100 Hz of frequency, and gain $K_0 = 100$. Operating in resonance (filter's and signal frequency are the same). Also, the interferometric signal ($y$) and the correction signal ($\phi_c$).

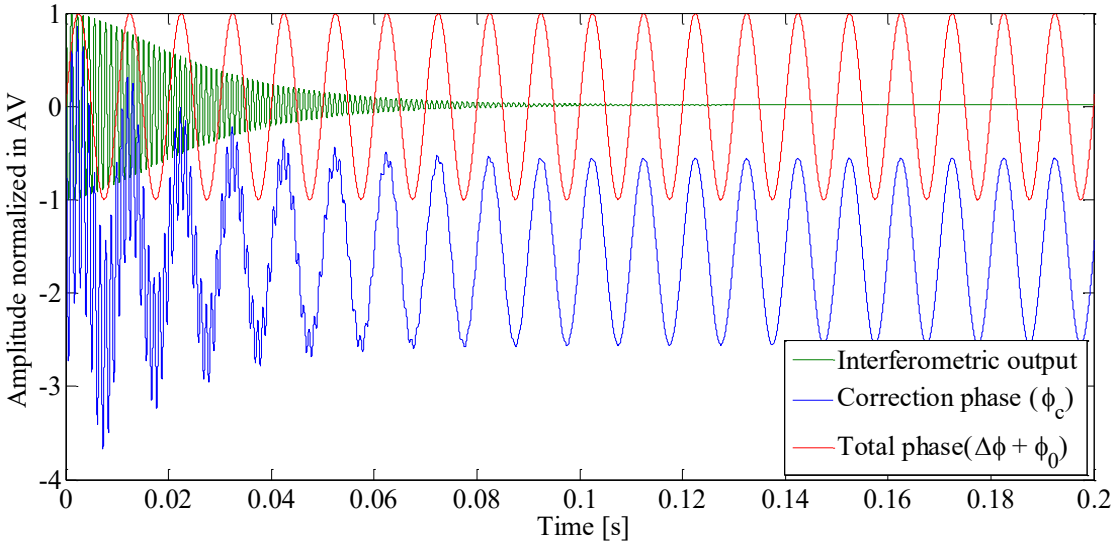


Source: from the author.

The system without switching has a similar operation when compared to the system with switching, although it converges faster with it than without it. In Figure 19 we can observe the interferometric output (in green) goes to zero about 0.1 seconds and in Figure 11, in 0.02 seconds. Also in Figure 19, the correction phase (in blue) follows the total phase, minus a bias around$-\pi/2$ (the closest equilibrium point), as expected.

Figure 20 shows the system without switching, now considering environmental disturbances: amplitude of $\phi_0$ equal to 2 V at 5 Hz, amplitude of $\Delta\phi$ equal to 1 V at $f_n = 100$ Hz and $K_0 = 200$.

Even in the presence of environmental disturbances the system is controlled. In Figure 20 we can see that the interferometric output (in green) goes to zero in about 0.05 seconds, being slower than the system with the switching (in Figure 12, the interferometric signal converges in less than 0.02 seconds). The correction phase also follows the total phase, and it also has a bias around$-\pi/2$. Therefore, one can observe that the system without switching also controls the plant: it is slower and loses robustness when compared to the system with switching, but controls the system within less operations and without the chattering effect (for higher gains).

Figure 20 - Closed loop control system (without switching) considering $\phi_0$ sinusoidal with 2 V and 5 Hz, for $\Delta\phi$ (interest signal) sinusoidal with 1 V and 100 Hz, and gain $K_0 = 200$. Operating in resonance (filter's and signal frequency are the same). Also, the interferometric signal ($y$), the correction signal ($\phi_c$) and the total phase ($\Delta\phi + \phi_0$).

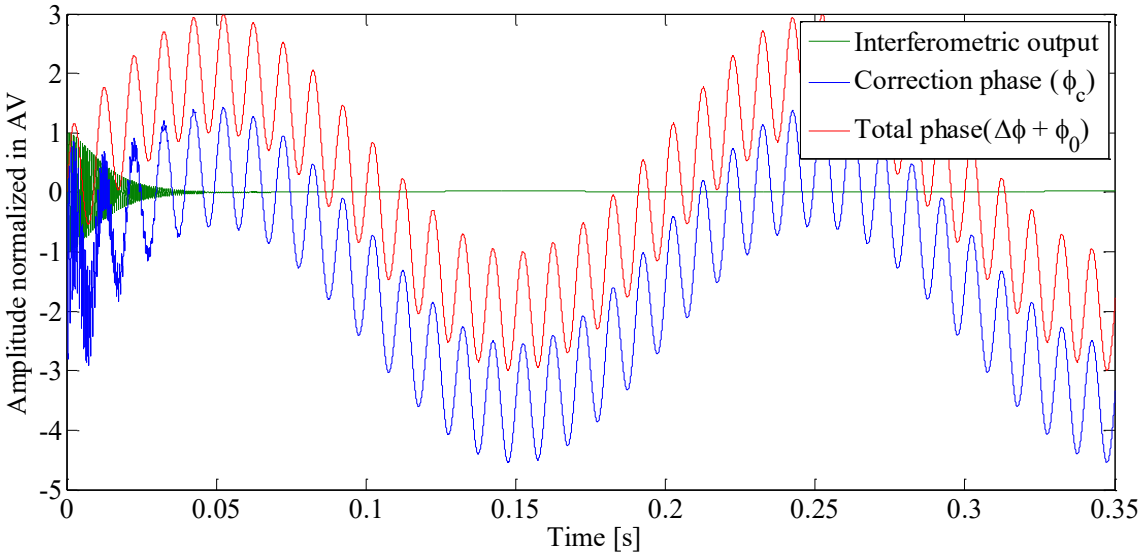


Source: from the author.

The control without switching was also tested in a discrete simulation, shown in next topic.

### *3.2.4.2 Discrete system's simulation*

For the simulation of the discrete system, the resonant filter needed to be rewritten to its discrete transfer function using the equation within the Z-Transform $\mathcal{Z}\{\cdot\}$:

$$G(z) = (1 - z^{-1})\,\mathcal{Z}\left\{\left(\mathcal{L}^{-1}\left\{\frac{G(s)}{s}\right\}\right)|_{t=kT_s}\right\}, \tag{43}$$

where $G(z)$ is the resonant filter transfer function for the discrete system, and $T_s$ the sampling period of the acquisition system (analog-digital converter). Applying (43) to (35), we can obtain:

$$G(z) = \frac{Bz+C}{z^2+Dz+1}, \tag{44}$$

and the parameters $B$, $C$ and $D$ are:

$$B = A - A\cos(\omega_n T_s) + \frac{1}{\omega_n}\sin(\omega_n T_s), \tag{45}$$

$$C = A - Acos(\omega_n T_s) - \frac{1}{\omega_n}\sin(\omega_n T_s), \tag{46}$$

$$D = -2cos(\omega_n T_s), \tag{47}$$

with $A = a/{\omega_n}^2$, and, for $a = {\omega_n}^2$, then $A = 1$ which corresponds to the resonant filter's gain. Also, $\omega_n$ is the resonant frequency and $T_s$, the sampling period.

Therefore, (44) - (47) are used to create the transfer function for the simulation, since it varies according to the sampling rate needed. So, Figure 21 shows the block diagram for the discrete simulation on Simulink.

Figure 21- Block diagram for the discrete simulation on Simulink.

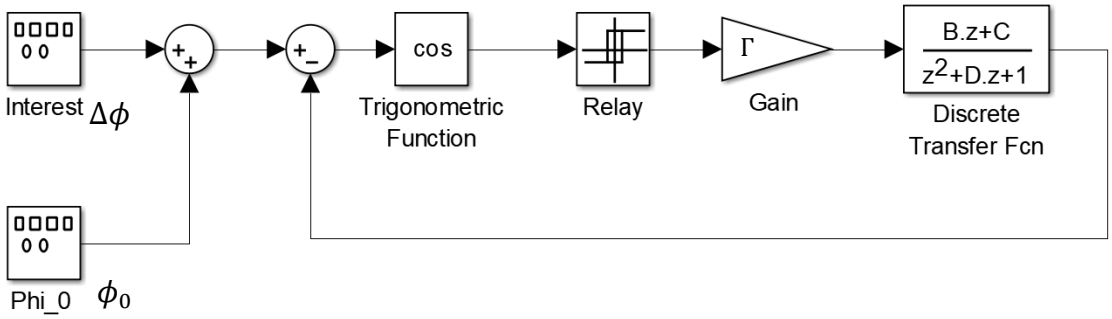


Source: from the author.

The discrete simulations show the importance of a minimum sampling rate, therefore tests were done for the minimum rate where the system could perform and the maximum resonance frequency of the filter could be set. We start with a physically reachable sampling frequency, 200 kHz, which would be the maximum sampling frequency of the myRIO.

Figure 22 - The interferometric signal ($y$) for the closed loop control system considering $\phi_0$ sinusoidal with 2 V and 5 Hz, for $\Delta\phi$ sinusoidal with 1 V and 55 Hz, gain of $\Gamma = 200$, resonance frequency at 55 Hz and sampling frequency at 200 kHz.

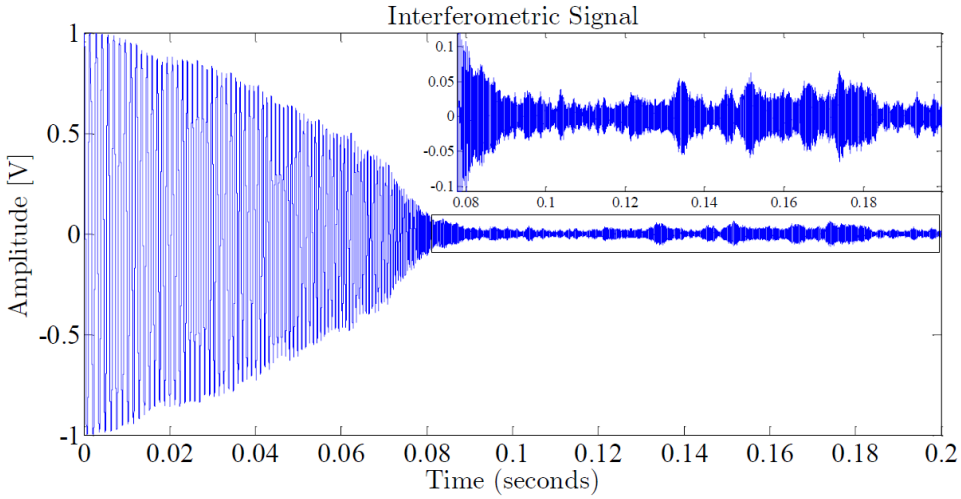


Source: from the author.

Under these conditions, and considering $\phi_0$ sinusoidal with 2 V and 5 Hz, $\Delta\phi$ sinusoidal with 1 V and 55 Hz, gain of $\Gamma = 200$, $f_n = 55$ Hz and $f_s = \frac{1}{T_s} = 200$ kHz, Figure 22 shows that the interferometric signal ($y$ in (16)) does not go totally to zero, but the control system still compensates (not properly, but it does).

Figure 23 - The correction signal and the total phase for the closed loop control system considering $\phi_0$ sinusoidal with 2 V and 5 Hz, for $\Delta\phi$ sinusoidal with 1 V and 55 Hz, gain of $\Gamma = 200$, resonance frequency at 55 Hz and sampling frequency at 200 kHz.

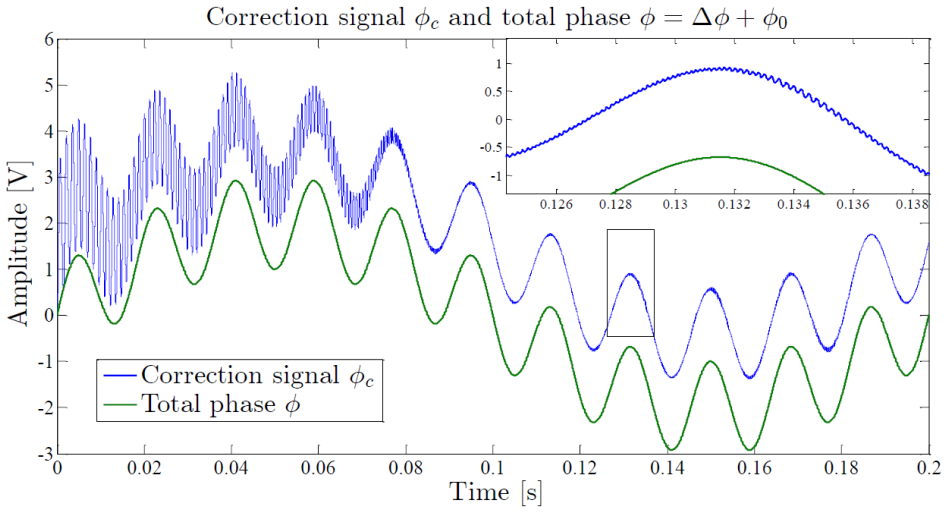


Source: from the author.

Observing the Figure 23, in the zoom area, one can observe that after the settling of the control (the correction signal following the total phase), the correction signal carries a tiny oscillation in a higher frequency, also the reason the interferometric signal from Figure 22 does not totally goes to zero, but oscillates around. The resonant frequency set can be considered a limit frequency for this sampling rate, once these oscillations were not supposed to appear. These facts indicate that the sampling rate needs to be increased.

For instance, the idea was to implement the physical feedback loop using the myRIO platform in real-time mode which has 200 kHz of sampling rate. Using two channels, the sampling rate reduces to 100 kHz, once we cannot guarantee that each channel will achieve the 200 kHz. Consequently, it would not be possible to implement not even a resonant filter at 50 Hz. For the same conditions, the sampling frequency was increased to 250 kHz (Figure 24). The FPGA available has this maximum sampling rate (250 kHz).

By increasing the sampling rate and maintaining the other parameters unchanged, Figure 24 shows that the oscillation around zero reduces almost 10 times when compared to Figure 22, so the oscillation in a higher frequency on the correction signal. This means that using a FPGA of 250 kHz, the maximum resonance frequency is 55 Hz.

Figure 24 - The interferometric signal ($y$) for the closed loop control system considering $\phi_0$ sinusoidal with 2 V and 5 Hz, for $\Delta\phi$ sinusoidal with 1 V and 55 Hz, gain of $\Gamma = 200$, resonance frequency at 55 Hz and sampling frequency at 250 kHz.

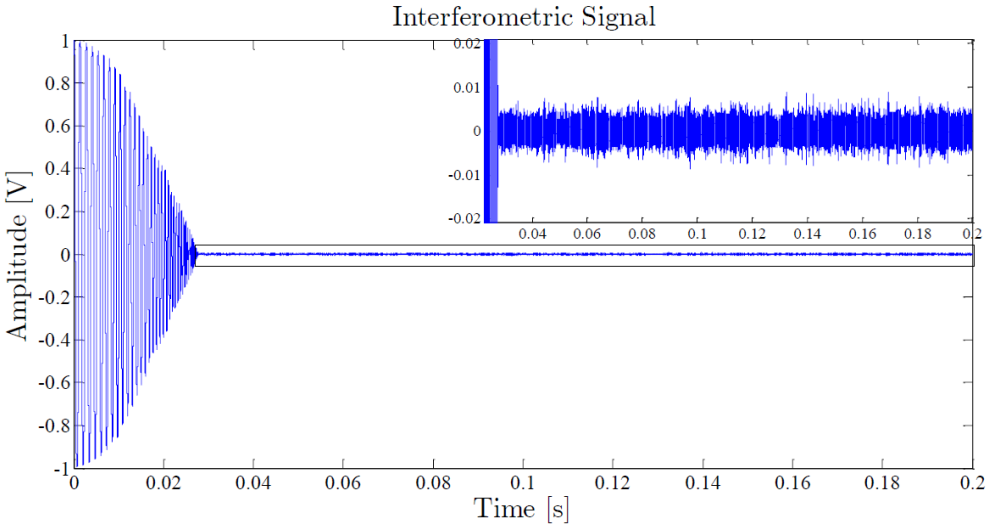


Source: from the author.

In Figure 25, we can observe the correction signal and the total phase for 250 kHz sampling frequency. In comparison to Figure 23, once the sampling rate is higher the oscillations seen in the correction signal are reduced.

Figure 25 - The correction signal and the total phase for the closed loop control system considering $\phi_0$ sinusoidal with 2 V and 5 Hz, for $\Delta\phi$ sinusoidal with 1 V and 55 Hz, gain of $\Gamma = 200$, resonance frequency at 55 Hz and sampling frequency at 250 kHz.

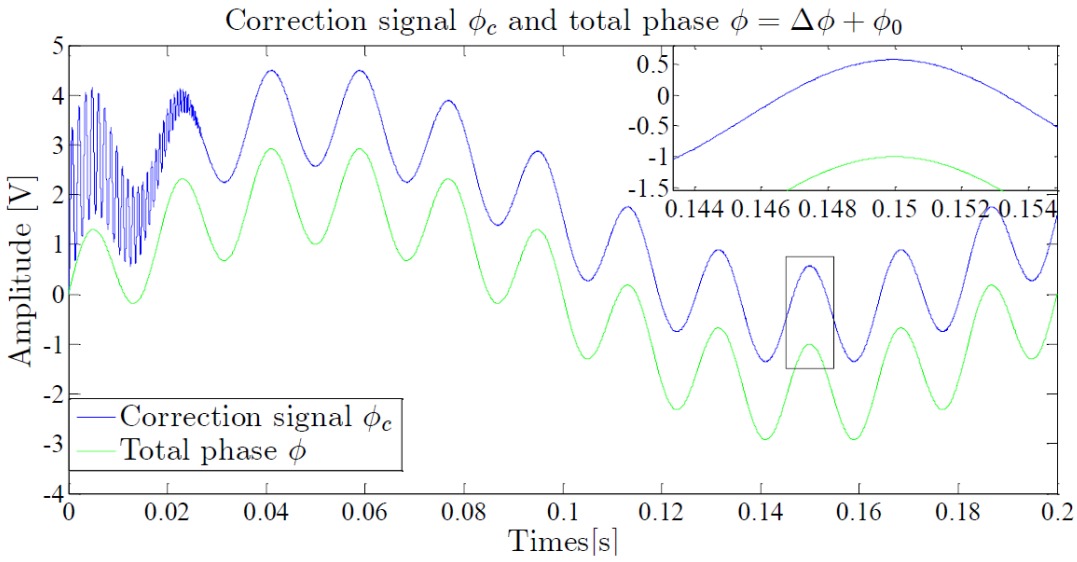


Source: from the author.

For that matter, we looked for the highest resonance frequency the filter could operate, giving the devices available. In order to close a physical feedback, we need at least two channels: an analog input and an analog output.

We had available the National Instruments (2015) MyRIO embedded platform (which can operate in real-time mode and FPGA), it could close the physical loop, but we cannot guarantee the sampling rate at its highest: for two channels the real time mode operates at 2 kHz at best, and the FPGA at 100 kHz. Therefore, the filter would resonate in a frequency lower than 50 Hz.

That being, the next device available would be the PCIe acquisition drive (also from *National Instruments*), which can achieve 1 MHz of sampling rate but it cannot close a physical loop once it is an acquisition drive. In order to achieve a sampling rate of at least 250 kHz, we propose in Chapter 4 (in the experimental setup section) to use Felão (2019) method of implementation that consist of the interferometer operating in open loop with a virtual track of the system, as will be explained in detail in the items ahead. For this method, we need at least 3 channels, therefore the maximum sampling rate is 333 kHz (guaranteeing no ghost

effect: no superposition of signals due gates with physically mutual voltage reference nodes). So, it is convenient to work in a sampling rate a bit smaller such as 300 kHz. For this rate, we tested the optimal resonance frequency of the filter, considering $\phi_0$ with 2 V and 5 Hz, $\Delta\phi$ with 1 V and 60 Hz, gain of $\Gamma = 200$, $f_n$ at 60 Hz and $f_s$ at 300 kHz. The simulation is ahead within Figure 26 and 36.

Figure 26 - The interferometric signal ($y$) for the closed loop control system considering $\phi_0$ sinusoidal with 2 V and 5 Hz, for $\Delta\phi$ sinusoidal with 1 V and 60 Hz, gain of $\Gamma = 200$, resonance frequency at 60 Hz and sampling frequency at 300 kHz.

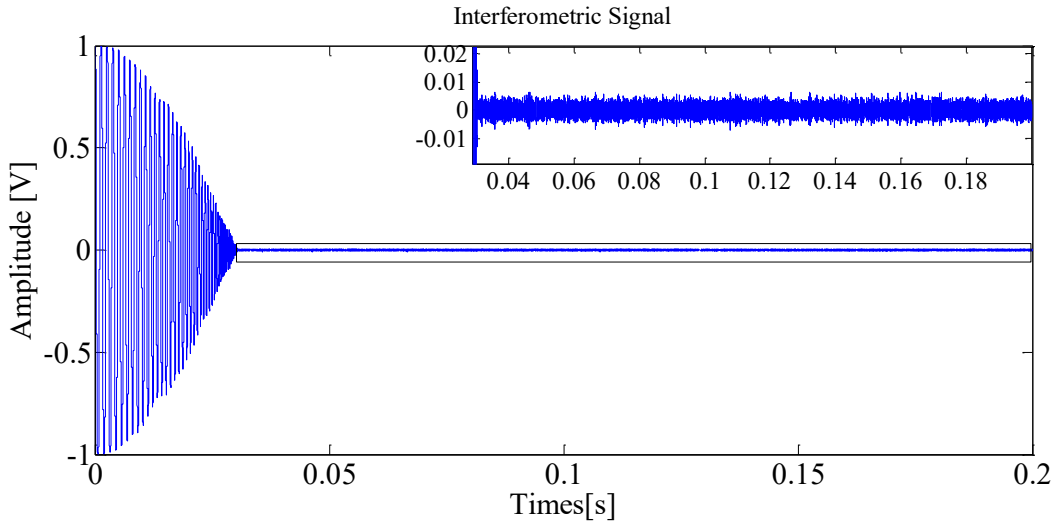


Source: from the author.

According to Figures 35 and 36, the highest resonance frequency is 60 Hz for 300 kHz of sampling rate.

Figure 26 shows a settling time of 0.03 seconds, and we also can see that the signal converges to zero within a range of less than |0.01| V, bring acceptable in relation to the signal amplitude at 0 seconds.

Figure 27 also presents the fact that the correction signal follows the total phase, as expected and stated before.

To illustrate, if the resonance frequency would a bit higher, as 70 Hz (Figure 28) or even 75 Hz (Figure 29), the system does not converge for 300 kHz sampling frequency.

Figure 27 - The correction signal and the total phase for the closed loop control system considering $\phi_0$ sinusoidal with 2 V and 5 Hz, for $\Delta\phi$ sinusoidal with 1 V and 60 Hz, gain of $\Gamma = 200$, resonance frequency at 60 Hz and sampling frequency at 300 kHz.

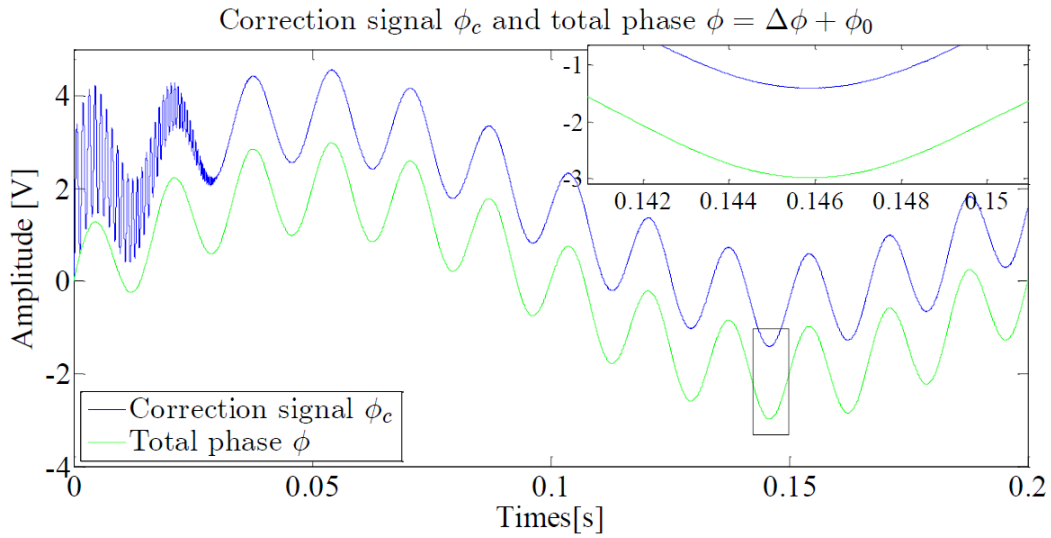


Source: from the author.

Figure 28 –The correction signal, the total phase and the interferometric signal for the closed loop control system considering $\phi_0$ sinusoidal with 2 V and 5 Hz, for $\Delta\phi$ sinusoidal with 1 V and 70 Hz, gain of $\Gamma = 200$, resonance frequency at 70 Hz and sampling frequency at 300 kHz.

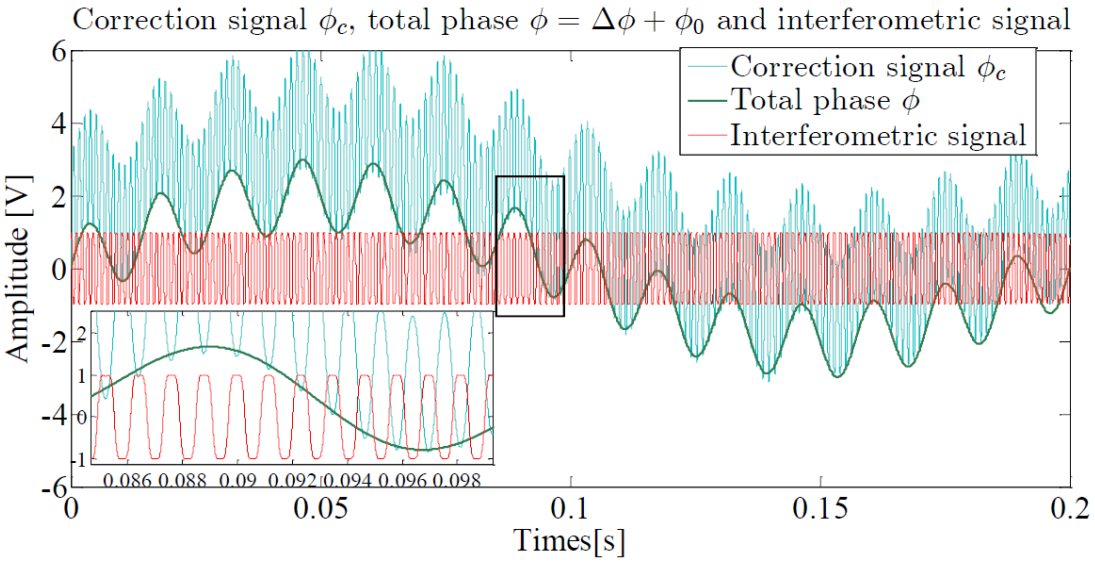


Source: from the author.

Figure 29 –The correction signal, the total phase and the interferometric signal for the closed loop control system considering $\phi_0$ sinusoidal with 2 V and 5 Hz, for $\Delta\phi$ sinusoidal with 1 V and 75 Hz, gain of $\Gamma = 200$, resonance frequency at 75 Hz and sampling frequency at 300 kHz.

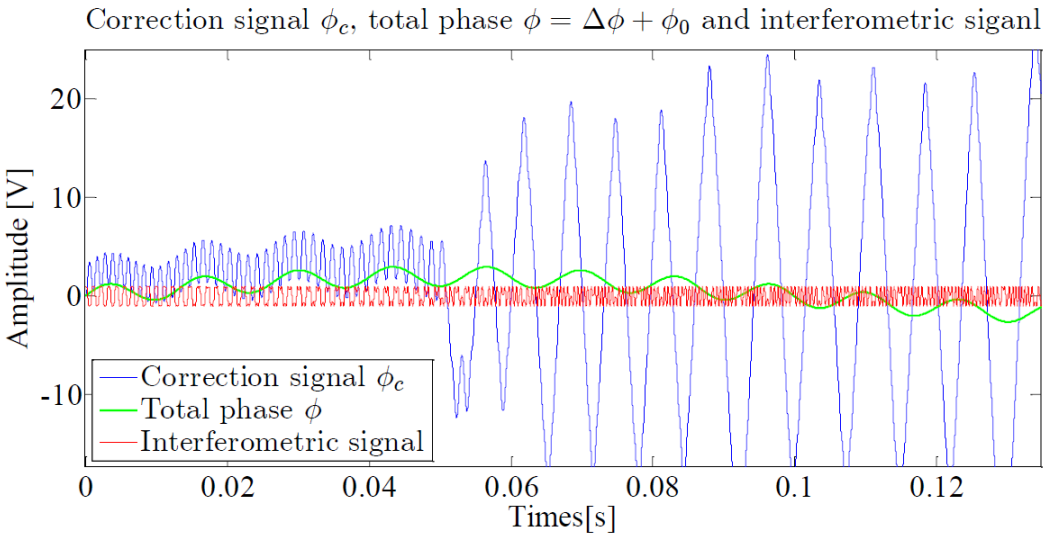


Source: from the author.

Figure 30 –The correction signal, the total phase and the interferometric signal for the closed loop control system considering $\phi_0$ sinusoidal with 2 V and 5 Hz, for $\Delta\phi$ sinusoidal with 1 V and 500 Hz, gain of $\Gamma = 200$, resonance frequency at 60 Hz and sampling frequency at 300 kHz.

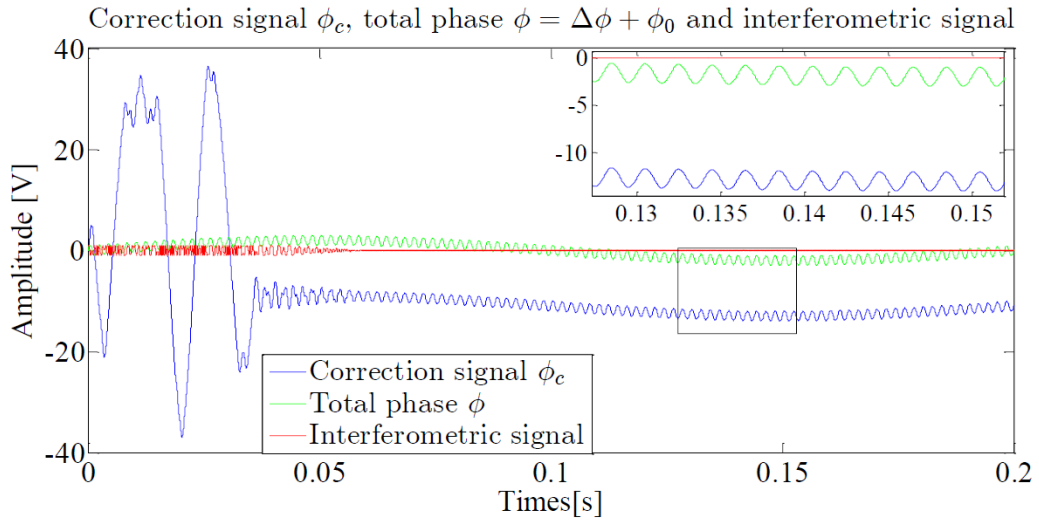


Source: from the author.

By this mean, all tests were done at 300 kHz of sampling rate and most with resonance at 60 Hz. This does not limit the high gain approach with a resonant filter to operate above those

frequencies, by increasing the gain (Γ) it is equivalent to elevate the magnitude curve from Figure 7, compensating even the frequencies above the resonance. Therefore, the far the frequency, the greater the gain would be. In the case of Figure 30, $\Gamma = 200$ was enough.

Figure 31 - The correction signal, the total phase and the interferometric signal for the closed loop control system considering $\phi_0$ sinusoidal with 2 V and 5 Hz, for $\Delta\phi$ sinusoidal with 1 V and 1000 Hz, gain of $\Gamma = 200$, resonance frequency at 60 Hz and sampling frequency at 300 kHz.

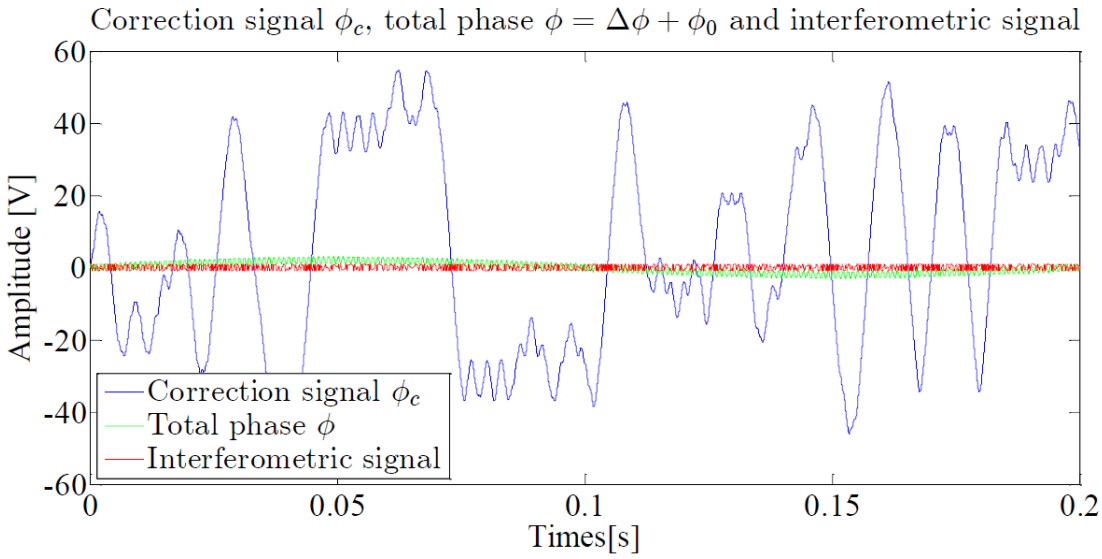


Source: from the author.

From Figure 30, where the conditions of simulations considers $\phi_0$ with 2 V and 5 Hz, $\Delta\phi$ with 1 V and 500 Hz, gain of $\Gamma = 200$, $f_n = 60$ Hz and $f_s = 300$ kHz. We can observe that the system takes almost 0.05 seconds (settling time) to reach a steady-state, and given the initial conditions the correction signal goes to a multiple of $-\pi/2$. But even out of resonance, the system fully compensates the total phase. And if we increase the gain, it will reduce the settling time.

Figure 31 shows the system operating with an interest signal at 1 kHz, maintaining the gain at $\Gamma = 200$. For that matter, the gain is not great enough to control the system, once the filter is out of resonance and according to Figure 8, it is attenuating the signal.

Increasing the gain to $\Gamma = 500$ is enough to compensate the system in the giving conditions (see Figure 32).

Figure 32 - The correction signal, the total phase and the interferometric signal for the closed loop control system considering $\phi_0$ sinusoidal with 2 V and 5 Hz, for $\Delta\phi$ sinusoidal with 1 V and 1000 Hz, gain of $\Gamma = 500$, resonance frequency at 60 Hz and sampling frequency at 300 kHz.

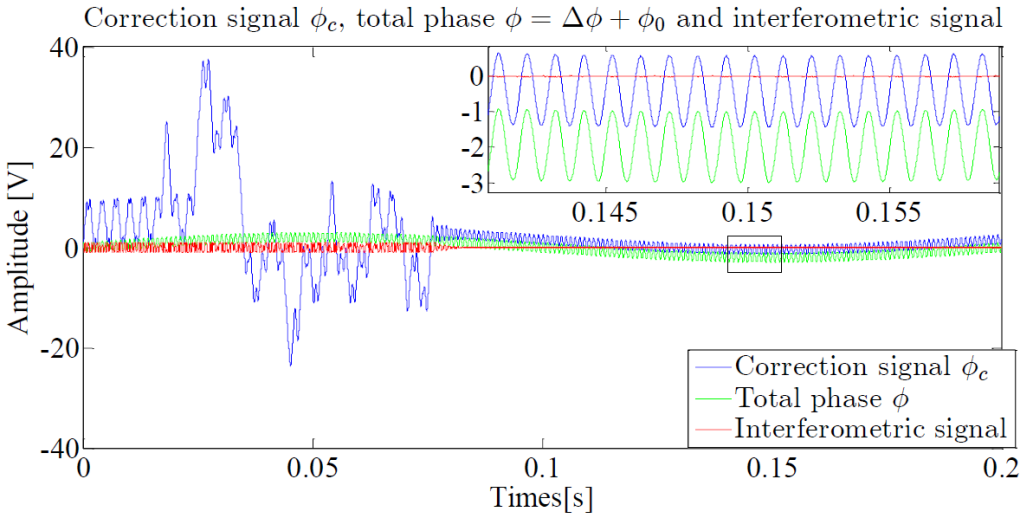


Source: from the author.

Figure 33 – System without switching in resonance: the correction signal, the total phase and the interferometric signal for the closed loop control system considering $\phi_0$ sinusoidal with 2 V and 5 Hz, for $\Delta\phi$ sinusoidal with 1 V and 60 Hz, gain of $K_0 = 400$, resonance frequency at 60 Hz and sampling frequency at 300 kHz.

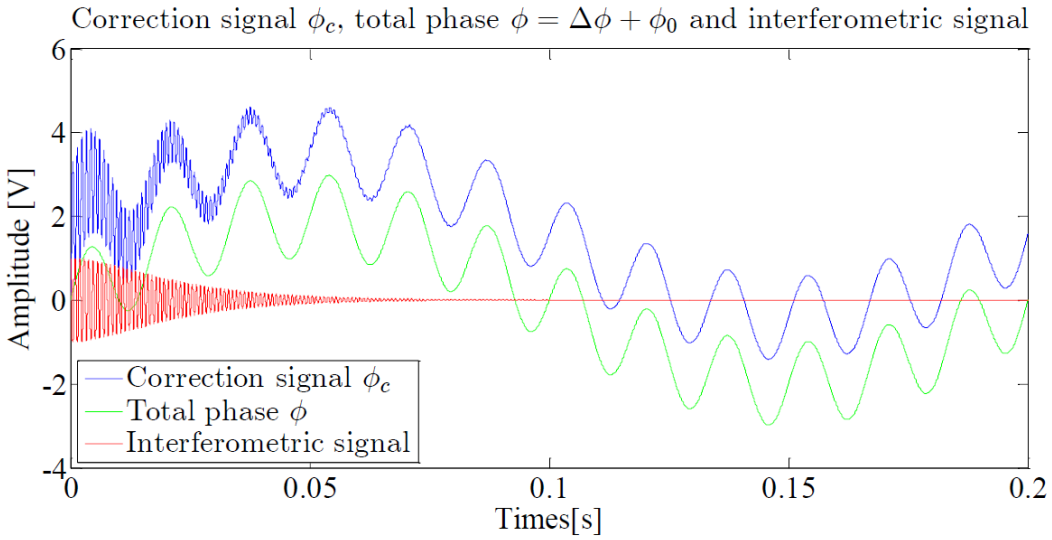


Source: from the author.

Source: from the author.

Figure 34 – System without switching out of resonance: the correction signal, the total phase and the interferometric signal for the closed loop control system considering $\phi_0$ sinusoidal with 2 V and 5 Hz, for $\Delta\phi$ sinusoidal with 1 V and 1000 Hz, gain of $K_0 = 80000$, resonance frequency at 60 Hz and sampling frequency at 300 kHz.

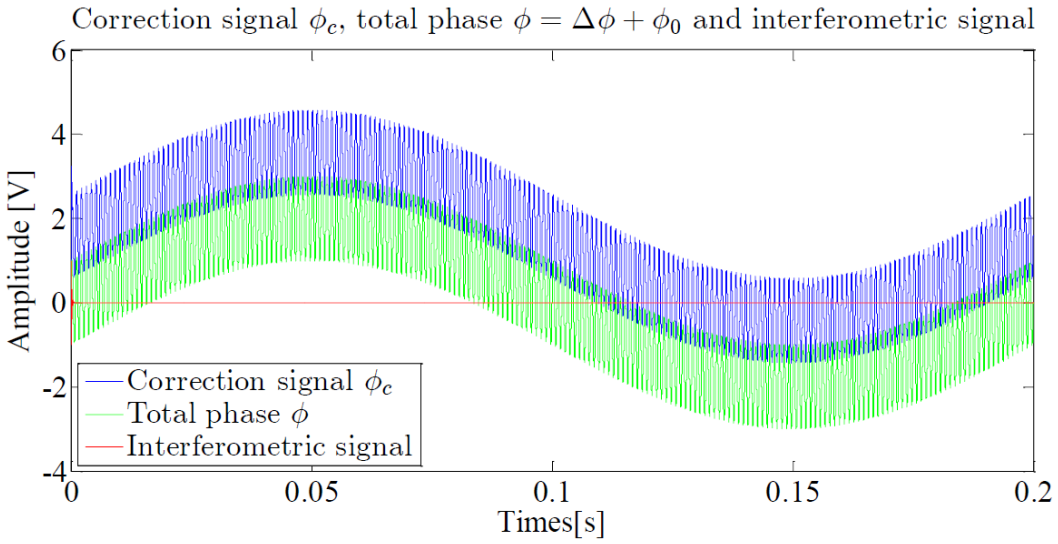


Source: from the author.

For both Figures 42 (considering $\phi_0$ with 2 V and 5 Hz, $\Delta\phi$ with 1 V and 60 Hz, gain of $K_0 = 400$, $f_n = 60$ Hz and $f_s = 300$ kHz) and 43 (considering $\phi_0$ with 2 V and 5 Hz, $\Delta\phi$ with 1 V and 1000 Hz, gain of $K_0 = 80000$, $f_n = 60$ Hz and $f_s = 300$ kHz), the gain was considered the minimum to take the interferometric signal to zero (and not an oscillation). It is noticeable that the system without switching needs a greater gain. It can operate perfectly, but if the gain would be a physical limitation there goes a disadvantage of the method. Once the implementation in this work is done digitally, the gain is not a problem.

Thereon, the system for the input (42) is presented in Figure 35.

Figure 35 - Block diagram for the discrete simulation on Simulink, system using both inputs.

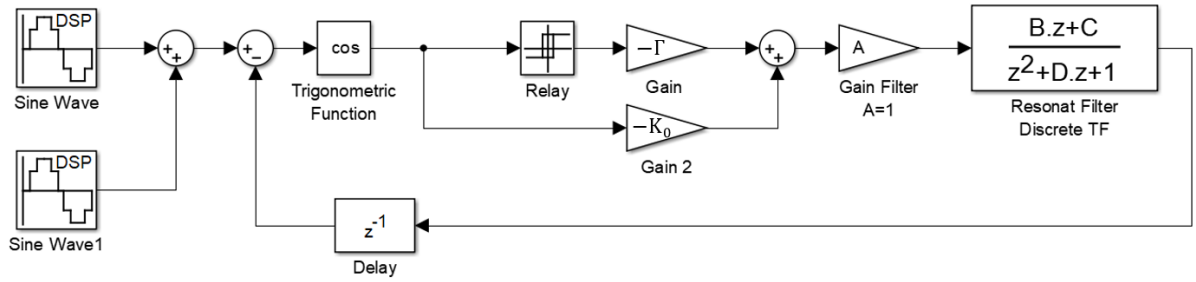


Source: from the author.

Figure 36 – System using both inputs, in resonance: the correction signal, the total phase and the interferometric signal for the closed loop control system considering $\phi_0$ sinusoidal with 2 V and 5 Hz, for $\Delta\phi$ sinusoidal with 1 V and 60 Hz, gain of $K_0 = 15$ and $\Gamma = 15$, resonance frequency at 60 Hz and sampling frequency at 300 kHz.

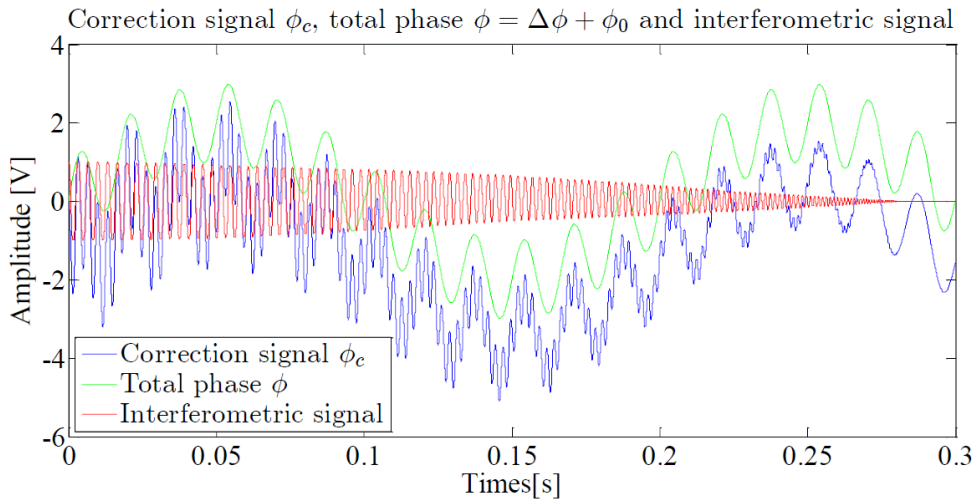


Source: from the author.

Figure 37 – System using both inputs, out of resonance: the correction signal, the total phase and the interferometric signal for the closed loop control system considering $\phi_0$ sinusoidal with 2 V and 5 Hz, for $\Delta\phi$ sinusoidal with 1 V and 1000 Hz, gain of $K_0 = 500$ and $\Gamma = 700$, resonance frequency at 60 Hz and sampling frequency at 300 kHz.

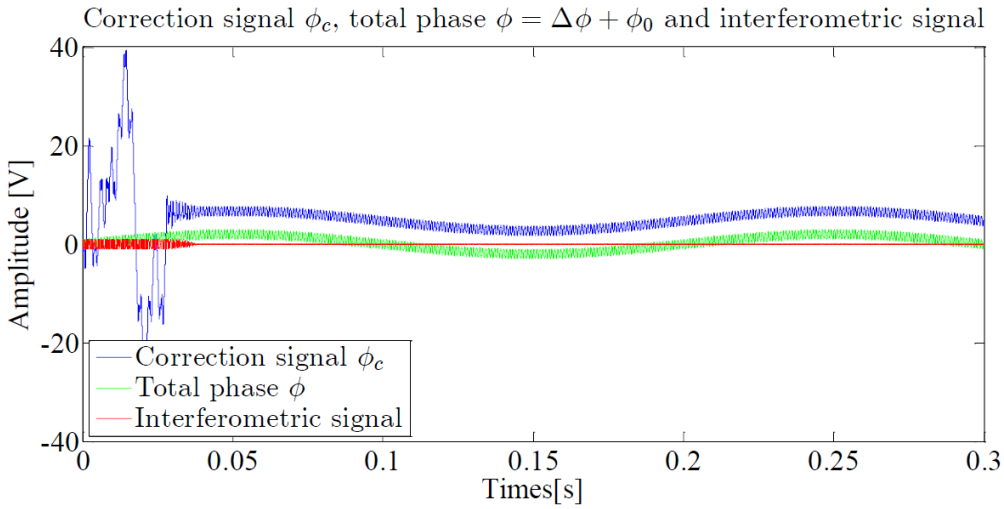


Source: from the author.

From Figures 45 (where it is considered $\phi_0$ with 2 V and 5 Hz, $\Delta\phi$ with 1 V and 60 Hz, $K_0 = 15$ and $\Gamma = 15$, $f_n = 60$ Hz and $f_s = 300$ kHz) and Figure 37 (where $\phi_0$

with 2 V and 5 Hz, $\Delta\phi$ with 1 V and 1000 Hz, $K_0 = 500$ and $\Gamma = 700$, $f_n = 60$ Hz and $f_s = 300$ kHz). One can observe that the system converges with a smaller gain, especially when in resonance. For comparison, in Table 1 is put together showing the gains of each system, for the same conditions.

Table 1 – Comparing minimum gain

| *Input* | $u = -\Gamma sgn(y)$ | $u = -K_0 y$ | $u = -K_0 y - \Gamma sgn(y)$ |
|---|---|---|---|
| *In resonance* $(60\ Hz)$ | 30 | 400 | $\Gamma = K_0 = 15$ |
| *Out of resonance* $(\Delta\phi\ at\ 1kHz)$ | 500 | 80000 | $\Gamma = K_0 = 500$ |

Next chapter will bring the description of the experimental setup and results.

# 4. EXPERIMENTAL SETUP AND RESULTS

This chapter brings the experimental setups and the discussion of the experimental results. The goal here is not only stabilizing the interferometric system as to ease the phase demodulation. To prove the method, we compare the results obtained with the controlled system to a classic method. The results are based on the displacement measure of a piezoelectric flextensional actuator (PFA) under evaluation.

## 4.1. EXPERIMENTAL SETUP

This section presents the block diagrams used to represent the experimental setup: the interferometer configuration and its connections to the acquisition system for the resonant filter controller (and all systems derived from it). As discussed in the simulations section, the resonant filter systems use Felão (2019) method of implementation, a tracking system that keeps the interferometer in quadrature and open loop (implementing a virtual controller).

The interferometer configuration is presented in Figure 38. It is a bulk Michelson interferometer with one of the mirrors coupled to an actuator to be studied (under evaluation). Also, the setup presents an extra beam splitter for signal quadrature's purpose.

Figure 38 – Experimental setup of the bulk Michelson interferometer

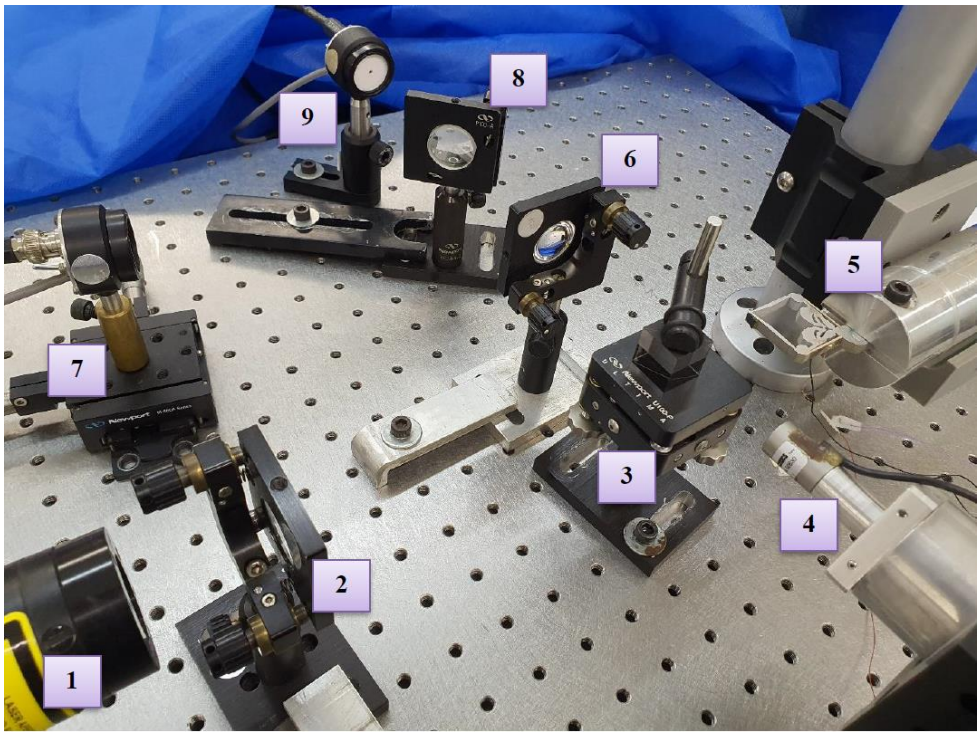


Source: from the author.

The interferometer was fixed on a Newport breadboard over the granite table, to ensure a better seismic isolation. The elements used are:

- [1] - He-Ne Laser source (Ealing Electrooptics, 5 mW) with wavelength 633 nm;
- [2] and [6] - Expander lenses to widen the beam diameter;
- [3] and [8] - Beam splitter with a 50/50 ratio;
- [4] – Reference mirror;
- [5] - Actuator under evaluation: the APFMA-XY;
- [7] and [9] - Photodetectors from ThorLabs (PDA55 Amplifier Si Photodetector, with bandwidth of 10 MHz and range of 400-1100 nm).

The piezoelectric flextensional actuator used in the rest of this work, the APFMA-XY (Figure 39), is one of several metallic structures hand over to FEIS-UNESP by the EPUSP Sensors and Actuators Group. Observing Figure 39, it is inferred that a compliant metallic structure allows the amplification of the motion generated by excited two PZTs. In addition, piezo ceramic coupling can be observed, as well as the terminals of the piezo ceramic for excitation, and the attached mirror on its surface. The coupling of a thin mirror to the structure is necessary for the reflection of the laser beam on the excited piece.

It is worth mentioning that this actuator tip has two points in which the displacements (in X and Y directions) are maximums. The tests performed in this work, characterized the behavior of the piezoelectric flextensional actuator in relation directly to point X (one of the two points conveniently named, for practical purposes). The practical applications of the actuators go from precision mechanics to medical applications (LE LETTY *et al*., 2003; NIEZRECKI *et al*., 2001), justifying their characterization. In this respect, laser interferometry is the most appropriate technique for this purpose.

Figure 39 – PFA under evaluation: APFMA-XY

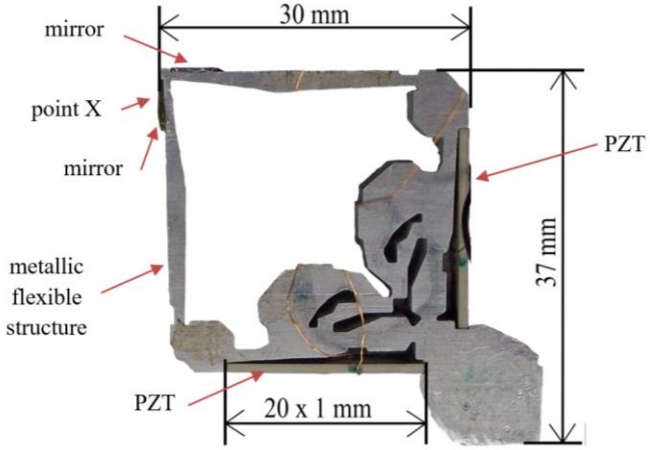


Source: from the author.

And since the digital control was programmed in LabVIEW (for all systems), we tried to implement using MyRIO (National instrument) in real-time mode but as shown in the simulations section, the sampling frequency was not enough for the resonant filter, so we implemented the system using Felão (2019) method and the PCIe acquisition driver (also from National Instruments, so the programming was all developed in LabVIEW).

### 4.1.1 Hardware and software used in the experimental setup

In order to present the project of the digital controlling system used, first we need to familiarize the basics on MyRIO-1900 embedded platform. Both hardware (MyRIO platform) and software (LabVIEW) were developed by National Instruments. LabVIEW stands for Laboratory Virtual Instruments Engineering Workbench. It is a high-level programming language. It uses a programming language, the G language, where the instructions are arranged in nodes and blocks of functions building the logic. It also has an improved graphical compiler to maximize system performance, making program development easier.

Virtual instruments, or VI's, are what are called the developed applications, because they present similarities to the physical instruments like oscilloscopes, digital multimeters, even signal generators. LabVIEW has a rich set of tools for data acquisition, analysis, processing, simulation, control, presentation and storage, as well as debugging tools.

The NI (National Instruments) embedded platform, myRIO-1900 (see Figure 40(a)) is a portable reconfigurable I / O (RIO) element. It is an embedded system with an ARM® Cortex ™ -A9 dual-core real-time processor and has customizable Xilinx FPGA (Field

Programmable Gate Array) inputs and outputs. It provides analog (AI / AO) inputs and outputs, as well as digital (DIO), audio and output sources in a compact and embedded device, and can be connected to a PC via USB or wireless port (see Figure 40 (b)).

Figure 40 – NI MyRIO. (a) device used. (b) block diagram.

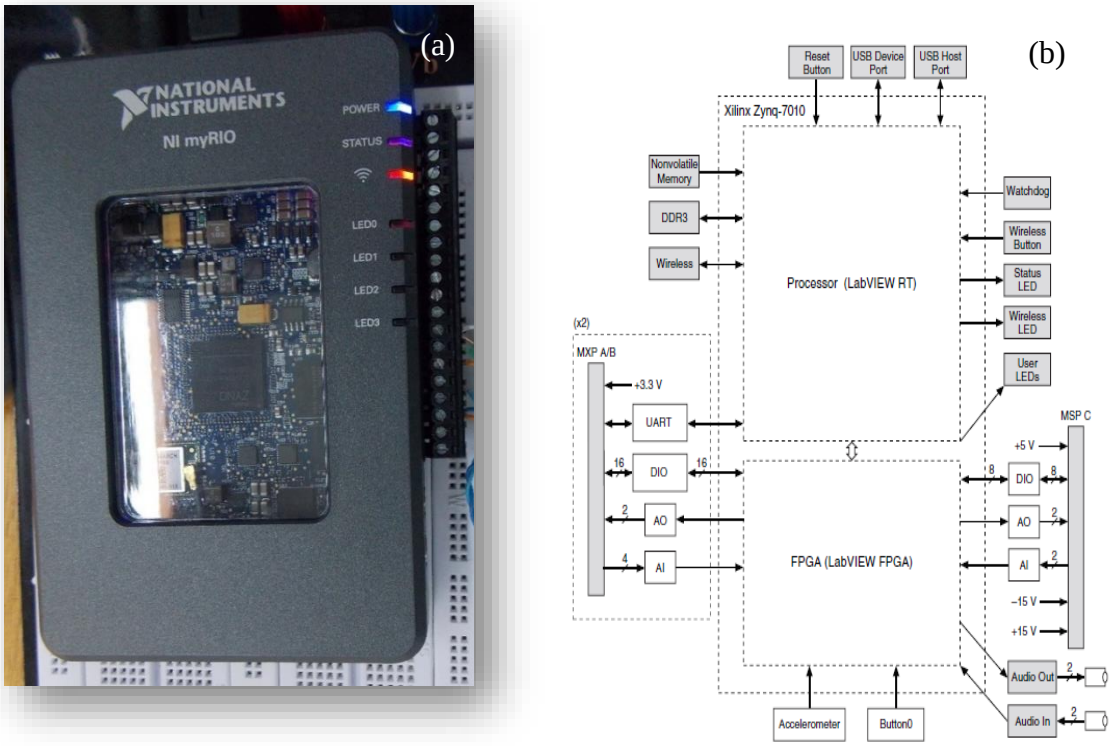


Source: (a) from the author. (b) National Instruments, 2015.

Consequently, one advantage to using MyRIO for control implementation is that even though the processing and acquisition of data is digital, it has the capability and speed to emulate the analog system feedback. In addition, it is more versatile than the analog system, since it has easy and intuitive parameter setting - given on the front panel, which is considerably simpler when compared to analog control, since for parameter changes it is necessary the minimum adjustment in potentiometers and trimpots, or until the exchange of components.

For the implementation using Felão (2019) method: with the system in open loop, the photodetected signals were acquired using the acquisition driver PCIe-6361 (connected to the computer) and the connector BNC-2090A (collecting the signals), both from *National Instruments* (Figure 41).

Figure 41 – Connection interface – BNC-2090A


Source: from the author.

The PCIe is an acquisition driver connected to computer in the rack of equipment and devices beside the optical table. It sends a pack of 200k samples to the program in the computer, which process the data pack.

The need of a high sampling rate (at least 250 kHz) justifies the use of this device, once it can achieve a sampling frequency of 1 MHz. For this setup, three inputs were used (AI0, AI1, AI2), therefore the sampling rate set in each channel was 300 kHz (with 3 channels it could go up to 333 kHz without warnings or ghost effect (superposition of signals)).

### 4.1.2 The virtual controller

Due the reasons presented, the equivalent system virtually controlled (Felão, 2019) was implemented, instead of a physical feedback loop. Thereby, the real system (physical interferometer) was used in quadrature and open loop according to Figure 4, while the feedback loop was virtually implemented in such way that the overall system is equivalent to the physically feedback interferometer. The feedback loop was implemented using LabVIEW (National Instruments).

In Figure 42, the Open-loop interferometer box represents the physical Bulk Michelson Interferometer. From its photodetectors the acquisition system acquires the signals at 300 kHz, in packages of 200k samples. The quadrature signals $v_{ac1}$ e $v_{ac2}$ go through an algorithm to correct the phase (Felão, 2019) between them, resulting a sine and a cosine. Using a trigonometric rule to obtain an interferometric signal, we have:

$$A_1V_1\cos(\phi_c+\phi) = A_1V_1\cos(\phi)\cos(\phi_c) - ((-A_1V_1\sin(\phi))(-\sin(\phi_c))). \quad (48)$$

After that, the interferometric signal goes through the control strategy and closes the feedback loop virtually (Figure 41).

The block diagram shown in Figure 42 synthesizes the interferometer behavior in a virtual manner, as well as the new proposal studied in Figure 5.

Figure 42 – The block diagram of the virtually implemented interferometer within the resonant system.

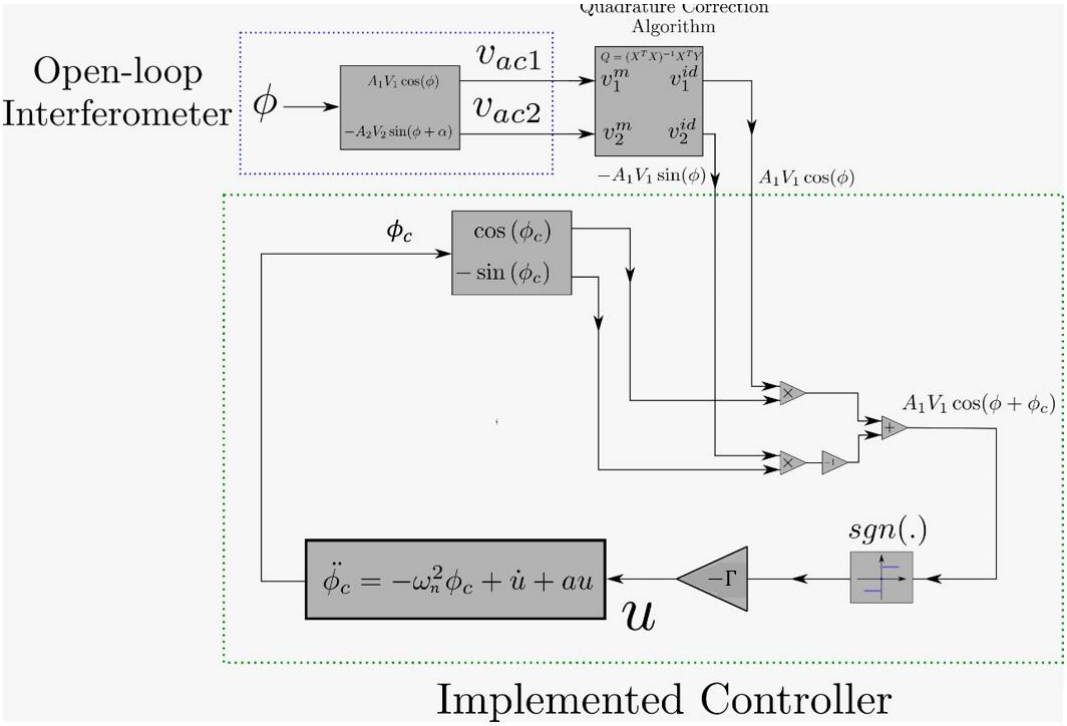


Source: modified from (FELÃO, 2019).

The virtual system proposed by Felão (2019) allows the implementation of any nonlinear control to the interferometer in quadrature: the ones already developed (MARTIN et. al, 2018; FELÃO, 2019) and the ones being proposed in this work. As the setbacks in this research appeared, we realize that using this method could help to implement the high gain systems. Unfortunately, so far in the research, only the resonant control system used this method of implementation. For future work, we intend to also use this method to implement the modified control system.

## 4.2 EXPERIMENTAL RESULTS

This section presents the experimental results for each setup. All the data was processed using Matlab software.

### 4.2.1 Resonant filter control systems

For the experimental set up presented in the last section, a series of tests were done to the systems. The tests were done at 300 kHz (sampling frequency). All the measurements were

done with high-modulation depth operation (around 1 to 2 V peak of the voltage generator, times the 20 V/V gain of the linear amplifier and using the APFMA-XY which has a 0.22 rad/V scale factor, resulting in a phase of 9.24 to 18.48 rad).

The recovered total phase shift is presented by two ways: using the correction phase ($\phi_c$) and the recovered phase using the classical method (arc tangent classical method or ATAN from (Lemes, 2014)) for the sake of comparison. The piezoelectric actuator APFMA-XY was evaluated in order to validate the method. And beside the systems presented in chapter 3, we also tested the system with the sigmoid instead of the sign function, in the end of this section.

The first system tested was the resonant filter with switching ($u = -\Gamma sgn(y)$), with the filter set in 50 Hz of resonance (input signal at the same frequency as the filter's) and controller gain (Γ) at 20. Figure 43 shows one of the interferometers output.

Figure 43 – Resonant filter with switching, operating at resonance (50 Hz, $\Gamma = 20$): Interferometric signal.

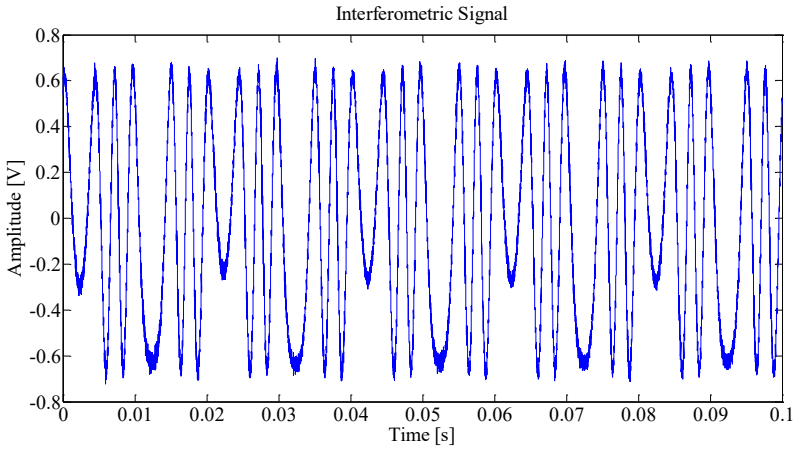


Source: from the author.

The interferometric signal shown in Figure 43 has a high modulation depth once the interferometer output signal is not proportional to a sinusoidal signal, as the next ones. It presents a visibly non-significant noise.

Figure 44 shows the total recovered phase using both methods to recover the phase: the correction signal using the virtually controlled system and the arc tangent classical method for the system operating in resonance, therefore the frequency of interest signal was set in the same frequency as the filter. The figures that shows the recovered interest signal are entitled with the term the recovered total phase shift, but during the data processing the quasi-static phase shift ($\phi_0$) is suppressed, therefore the signals shown are $\Delta\phi$ ($\phi_c = \Delta\phi$ for the recovered

signal using the virtual controlling system, and $\Delta\phi$ calculated throughout data processing using the arc tangent algorithm).

Figure 44 – Resonant filter with switching, operating at resonance (50 Hz, $\Gamma = 20$): Recovered total phase shift.

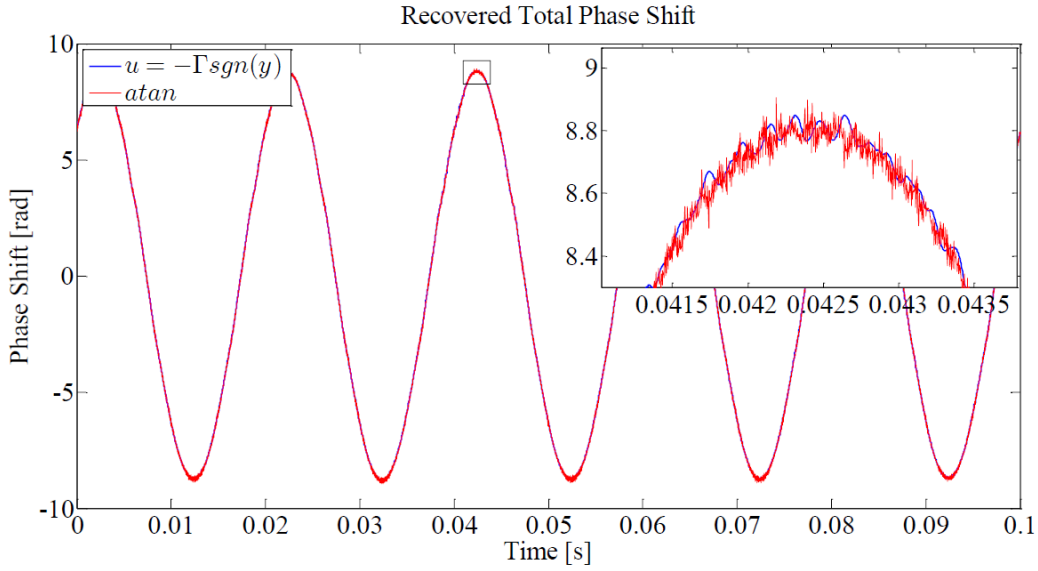


Source: from the author.

From Figure 44 we can observe that the ‘atan’ method carries the noise from the input (Figure 43) to the outcome (curve in red). And the control system actually filters the signal at 50 Hz with it the noise. The oscillations presented in the curve in blue are due the small gain value of (Γ) (as forseen in chapter 3, once the gain (Γ) is not enough this oscilations appear).

Figures 45 and 46 present the same system operating out of resonance (interest signal at 500 Hz, and filter at 50Hz). Due the system operation out of resonance, the controller gain (Γ) needs to be increased, assuming $\Gamma = 1{,}000$ .

Figure 45 – Resonant filter with switching, operating out of resonance (signal at 500 Hz, filter at 50 Hz, $\Gamma = 1{,}000$): Interferometric signal.

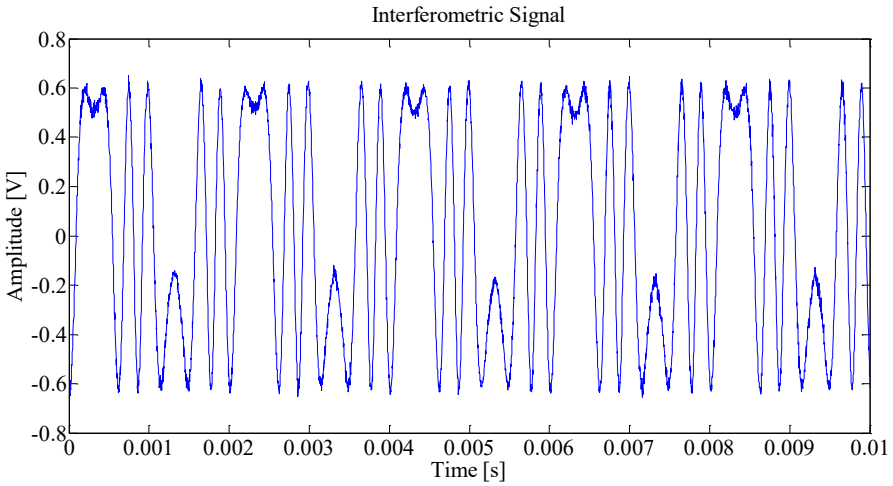


Source: from the author.

Comparing Figure 45 to Figure 43, both images show the interferometric signal whereas the input is greater than $\pi/2$ rad, thereby a high modulation depth. Both figures are one of the two signals photodetected and acquired by the driver.

Figure 46 – Resonant filter with switching, operating out of resonance (signal at 500 Hz, filter at 50 Hz, $\Gamma = 1{,}000$): Recovered total phase shift.

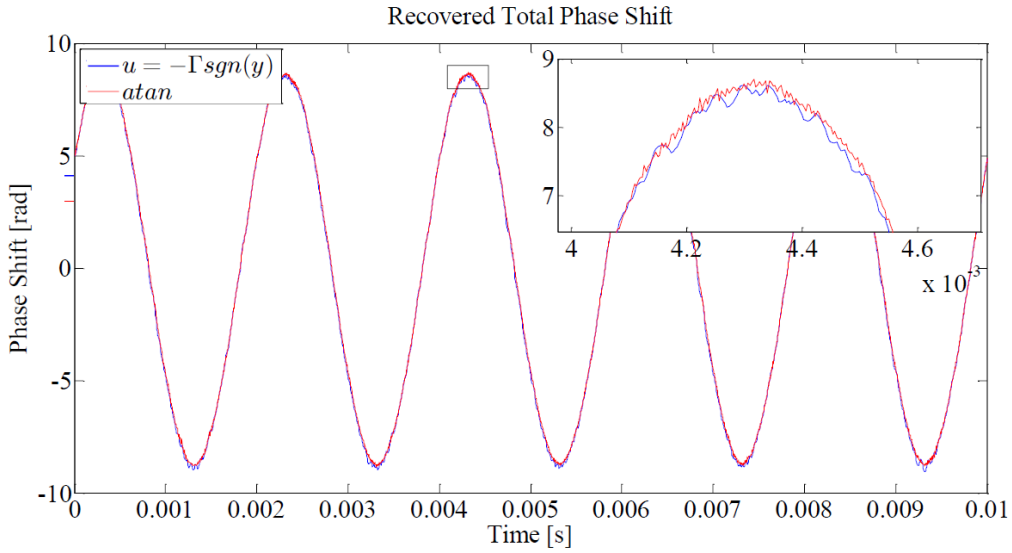


Source: from the author.

From Figure 46, one can conclude that the system also works out of resonance, giving a greater gain (Γ). Using this system, the frequency response of the PFA APFMA-XY was taken.

Figure 47 – Frequency Response (Magnitude) of the APFMA-XY: Resonant filter with switching and arc tangent.

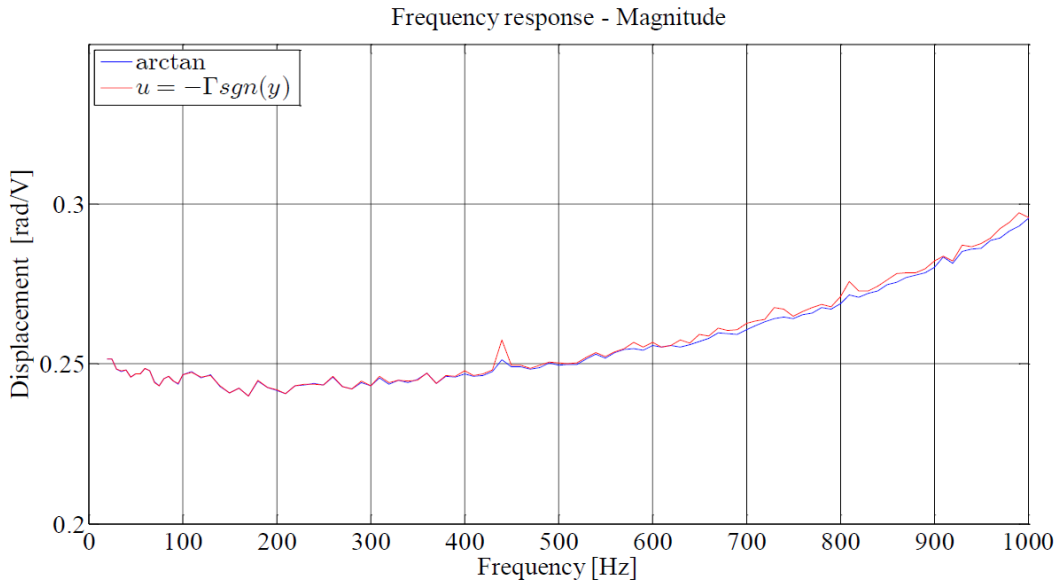


Source: from the author.

The responses agree specially in the lower frequencies (near the filter's resonance), once we get far from the filter's resonance the gain (Γ) needs a boost and the system can become instable due the chattering effect (once we have a switching) and the curves in Figure 47 stars to have a small difference (a discrepancy plot is shown by the end of this chapter). The method is valid when compared to the arc tangent classic method.

The measurements were done till 2,000 Hz, but in Figure 47 (magnitude of the scale factor) were only shown till 1,000 Hz because after that the gain needs to be greater and we have a mechanical resonance of the APFMA-XY around 1,800 Hz (as can be seen in Figure 48) where the controlling systems has the need to increase the controller gain (Γ) till the system can no longer compensate the entire phase.

In Figure 47, around 450 Hz we can spot a peak of the response taken with the control system that differs the response calculated with the arc tangent algorithm. This peak can happen when the system has a switch in the equilibrium point due a physical perturbation and signal correction is a signal proportional to the interest signal but with a change of bias (from one equilibrium point to another due perturbation). Once the data processing to obtain the frequency response calculates the amplitude of the signal (a maximum to a minimum point), there might be a mistake in processing, catching a minimum from a lower equilibrium point and the maximum of a greater equilibrium point, causing this kind of discrepancy. To make

sure this doesn't happen it is advised to full proof the algorithm of data processing against this sort of mistake.

Figure 48 – Frequency Response (Phase) of the APFMA-XY: Resonant filter with switching and arc tangent.

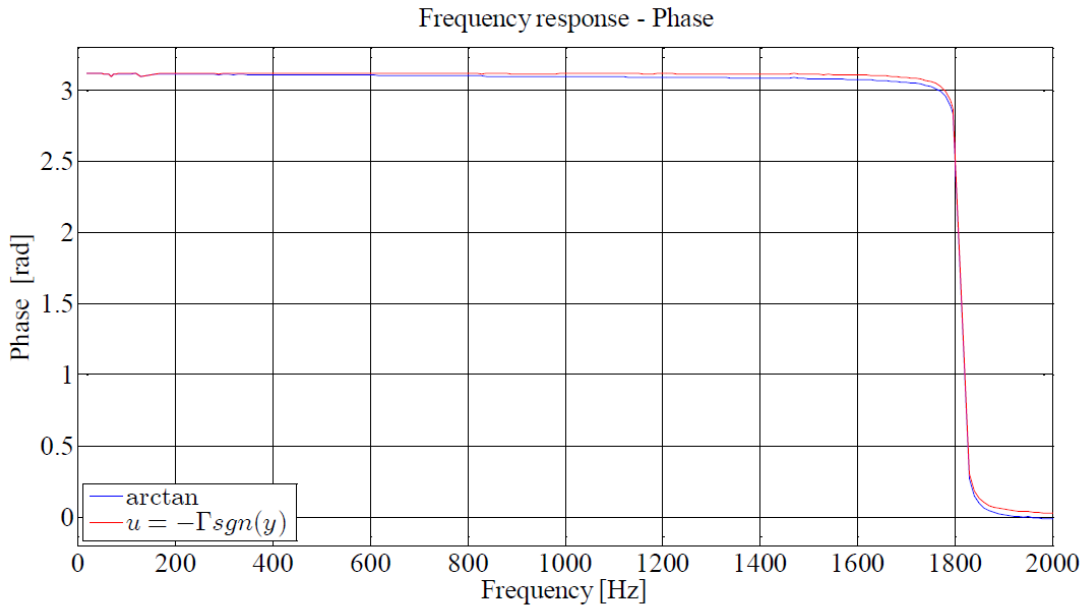


Source: from the author.

The method is also to validated to measure phase (due to the delay introduced by the APFMA-XY piezo ceramics), as seen in Figure 48, once the curves agree. Also, the phase shift from $\pi$ to 0 rad at 1,800 Hz, represents a mechanical resonance of the actuator (expected). This mechanical resonance was not plotted in the magnitude graphic once the gain (Γ) was too great (over 200k) that lead the system divergences, being that the reason all frequency responses that follow were done till 1 kHz (as mentioned before).

Figure 49 demonstrates the effects of being far from the filters resonance. With the input signal at 1,700 Hz, the filter kept at 50 Hz (as discussed in the simulations section) and since the signal is at a frequency so far from the resonance the gain (Γ) goes to 14,000 value. Observing Figure 49 we can see that when close to de the mechanical resonance, the phase to compensate starts to increase rapidly, therefore the gain also need a boost (also because the mechanical resonance (1800 Hz) happens far from the filters resonance (50Hz)). So, the recovered phase starts to have some discrepancy in the sinusoidal waveform when compared to the classic method.

Figure 49 - Resonant filter with switching, operating out of resonance (signal at 1,700 Hz, filter at 50 Hz, $\Gamma = 14{,}000$): Recovered total phase shift.

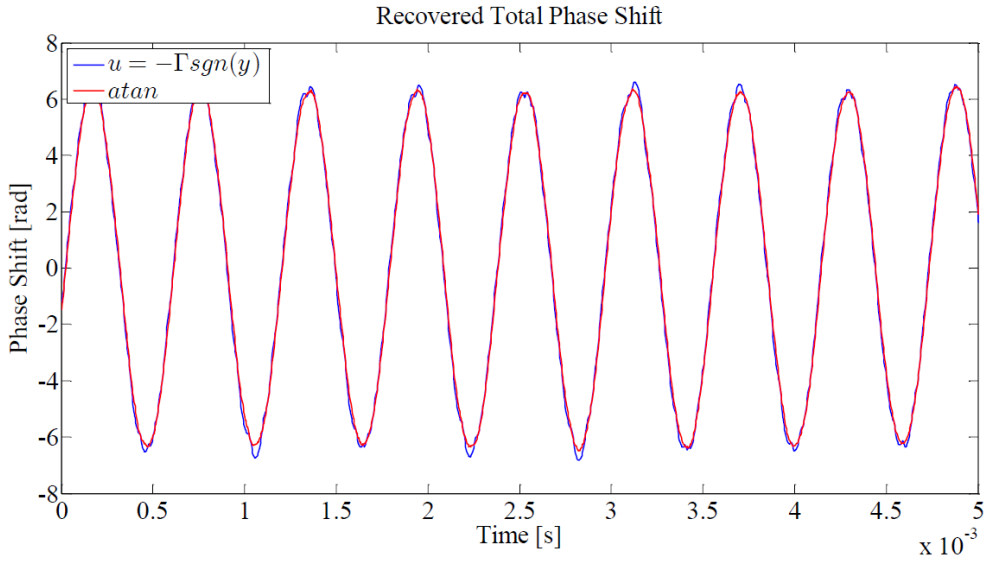


Source: from the author.

Now, presenting the tests done for the system without switching ($u = -K_0 y$) for the same experimental setup (same actuator, same interferometer, just taking off the switching block of the system). Firstly, the recovered total phase shift in resonance (Figure 50) with the resonance frequency set at 50 Hz for the filter and the signal, and the gain of controller at $K_0 = 100$.

Figure 50 - Resonant filter without switching, operating at resonance (50 Hz, $K_0 = 100$): Recovered total phase shift.

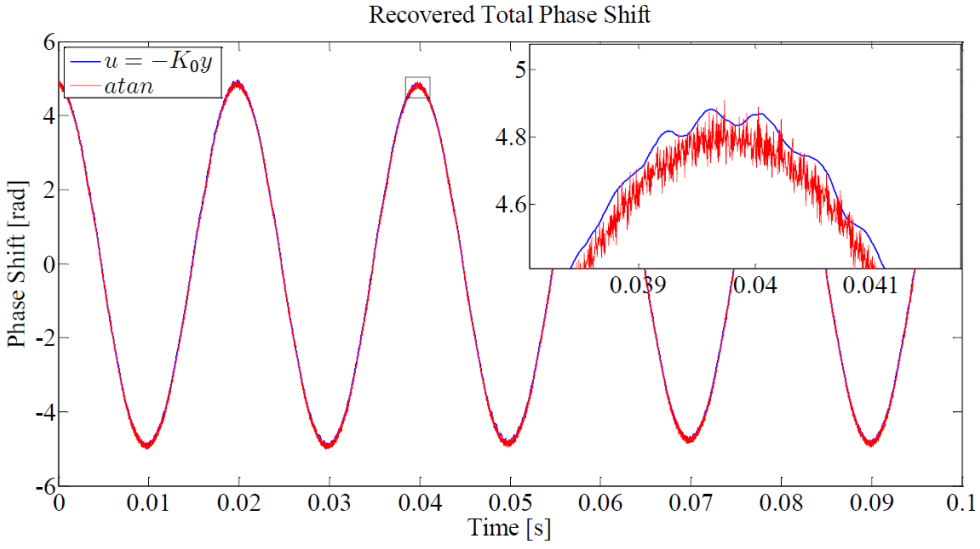


Source: from the author.

Afterwards, the recovered total phase shift out of resonance (Figure 51) with the resonance frequency set at 50 Hz for the filter and the signal at 290 Hz, the gain of controller at $K_0 = 1{,}000$.

Figure 51 – Resonant filter without switching, operating out of resonance (signal at 290 Hz, filter at 50 Hz, $K_0 = 1{,}000$): Recovered total phase shift.

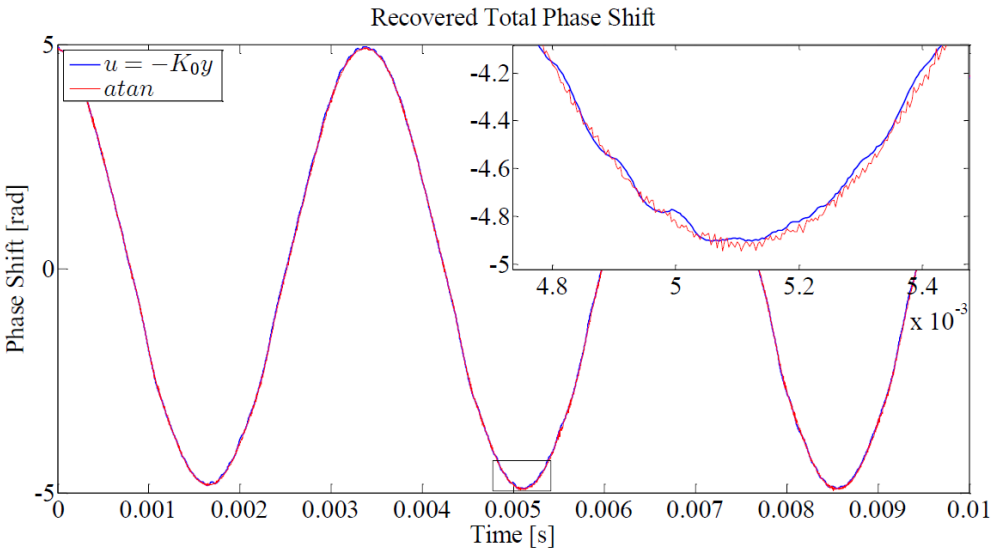


Source: from the author.

From Figure 50 with $K_0 = 100$, and Figure 51 $K_0 = 1{,}000$, we can see that the recovered phases agree with the arc tangent classic method even when out of resonance. The system is not as robust as the previous one (because of the absence of the switching), but it has a different relation to the gain (it does not take the system to instability but needs to be greater than the required previously). For example, in the system with switching the gain for 500 Hz was set in $\Gamma = 1{,}000$, and for the system without it and same frequency, the gain was $\Gamma = 10{,}000$ (ten times greater).

In the same matter, the response of the APFMA-XY was measured using the system controlled without switching and compared to the arc tangent classical method. Figure 52 shows the magnitude of the frequency response till 1,000 Hz regarding these considerations.

Figure 52 – Frequency Response (Magnitude) of the APFMA-XY: Resonant filter without switching and arc tangent.

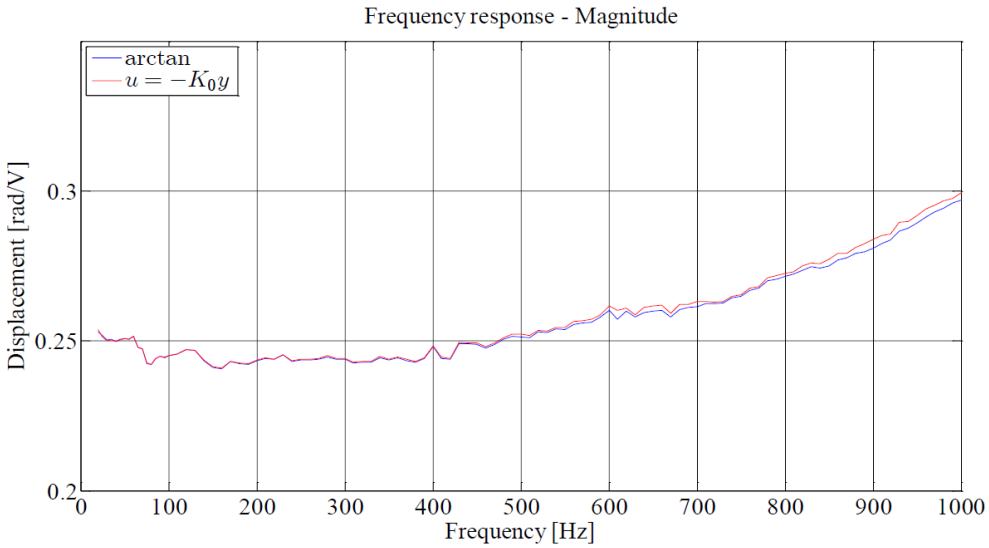


Source: from the author.

From Figure 52, we can observe that the curve agrees as well, and due the frequency of resonance be in lower frequency (50 Hz), the far the frequency gets the greater the difference between the curves (yet small when calculated the error).

The phase was also plotted in Figure 53.

Figure 53 – Frequency Response (Phase) of the APFMA-XY: Resonant filter without switching and arc tangent.

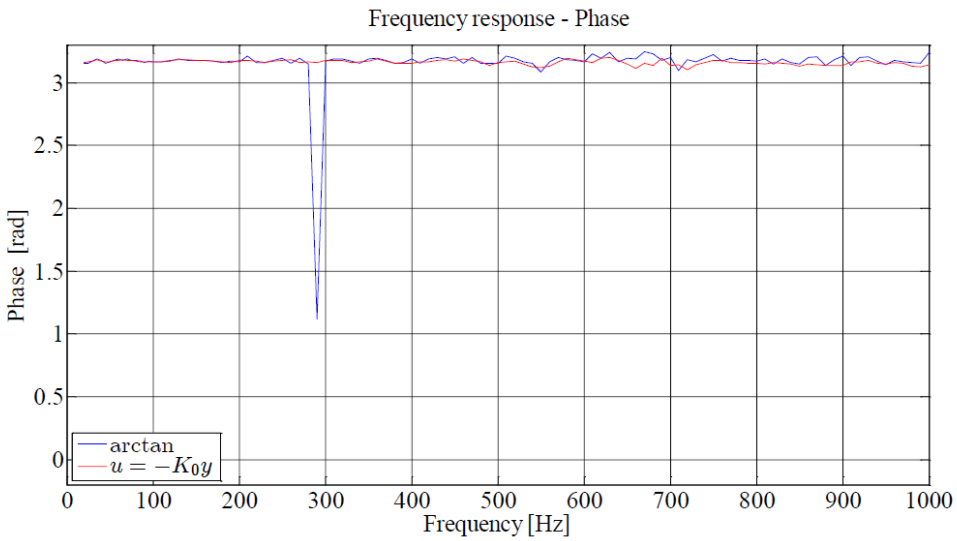


Source: from the author.

When compared to the previous response shown in Figure 48, Figure 53 has the same behavior except the frequency around 290 Hz where the classic method (in blue) assumes a different value of high discrepancy. That being an error of classic method.

The complete system (using both inputs, $u = -\Gamma sgn(y) - K_0 y$) was tested, again, for the same physical setup, with changes only in the virtual controller concerning the filter input. The conditions of amplitude of the interest signal remains the same as described in the beginning of this section.

Figure 54 shows the recovered phase shift at resonance. For this tests, the interest signal ($\Delta\phi$) has a frequency of 50 Hz and resonant frequency also at 50 Hz), with the controller gains $\Gamma = K_0 = 1{,}000$.

Figure 54 - Resonant filter with both inputs, operating at resonance (50 Hz, $\Gamma = K_0 = 1{,}000$): Recovered phase shift.

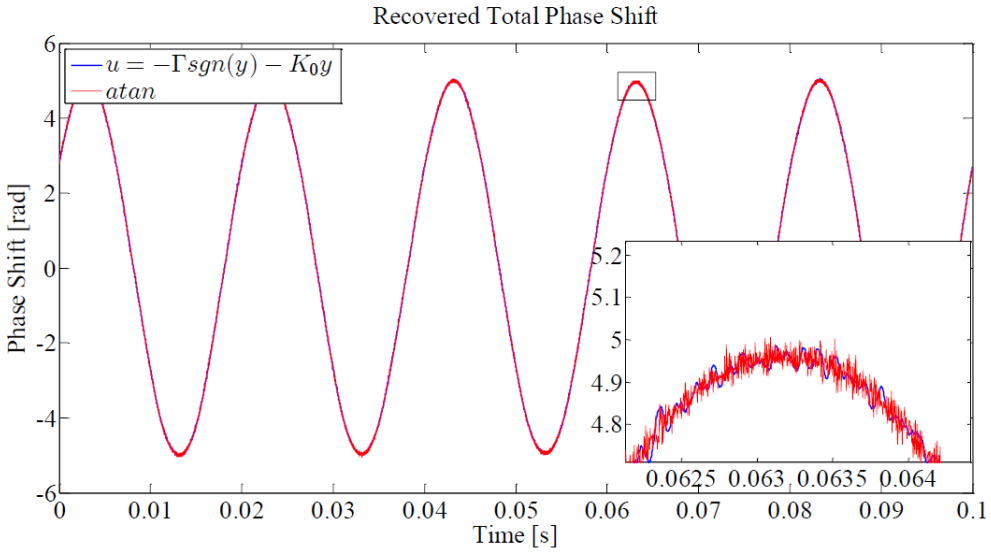


Source: from the author.

Figure 54 shows the recovered phase shift out of resonance, therefore the interest signal is at 500 Hz and the resonance frequency of the filter is at 50 Hz, with the controller gains $\Gamma = K_0 = 5{,}000$.

Figure 55- Resonant filter with switching, operating out of resonance (signal at 500 Hz, filter at 50 Hz, $\Gamma = K_0 = 5000$): Recovered total phase shift.

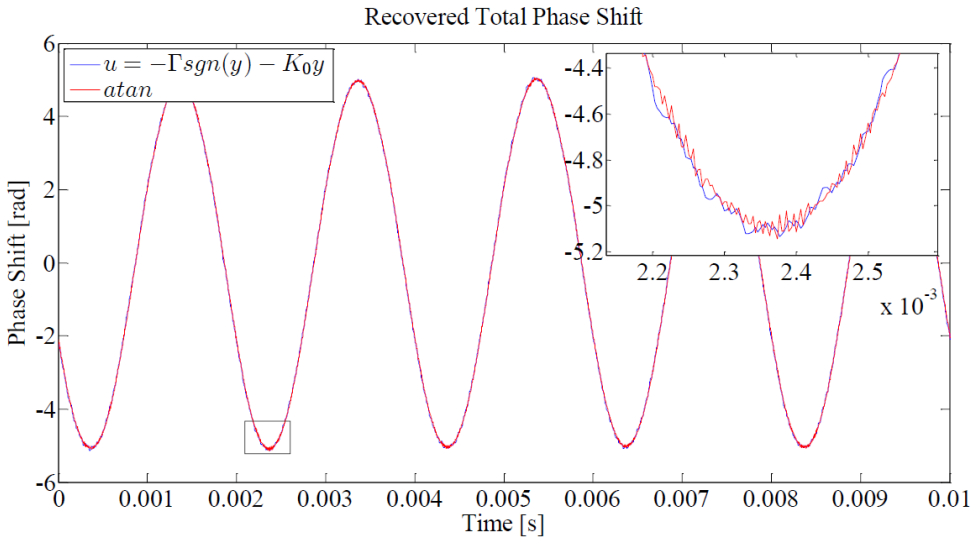


Source: from the author.

So, the system with both input has a gain region in between methods. And during the tests we find out that is better to have the same gain for Γ and $K_0$. The recovered phases from Figures 54 and 55 maintain the pattern seen in the previous recovered phases, where the controlling signal does not carry out the noise as the arc tangent method does.

The tests of the system with both inputs ($u = -\Gamma sgn(y) - K_0 y$) had very similar responses, and the idea behind this association was to reduce the gain applied in the controller (once the system without switching had a greater gain for similar frequencies bands than the system with switching), for the matter, the part of the input that has the switching ($-\Gamma sgn(y)$) would dominate the higher frequency (often to be the interest signal, $\Delta\phi$) which needs a greater gain to compensate these frequencies, and when operating in sliding mode has, to what we consider, an infinite gain at the switching. Whereas the part of the input without the switching ($u = -K_0 y$) comes to dominate the lower frequencies such as the environmental disturbances (as the quasi-static phase, $\phi_0$).

Due the outcome, the frequency response of the APFMA-XY was also evaluated.

Figure 56 presents the magnitude of the frequency response of the APFMA-XY, using the virtually controlled system (with both inputs) and processed by using the arc tangent method. Also, Figure 57 shows the phase delay of the frequency response for the APFMA-XY. Both Magnitude (Figure 56) and Phase (Figure 57) frequency response have 1,000 Hz.

Figure 56 – Frequency Response (Magnitude) of the APFMA-XY: Resonant filter both inputs and arc tangent.

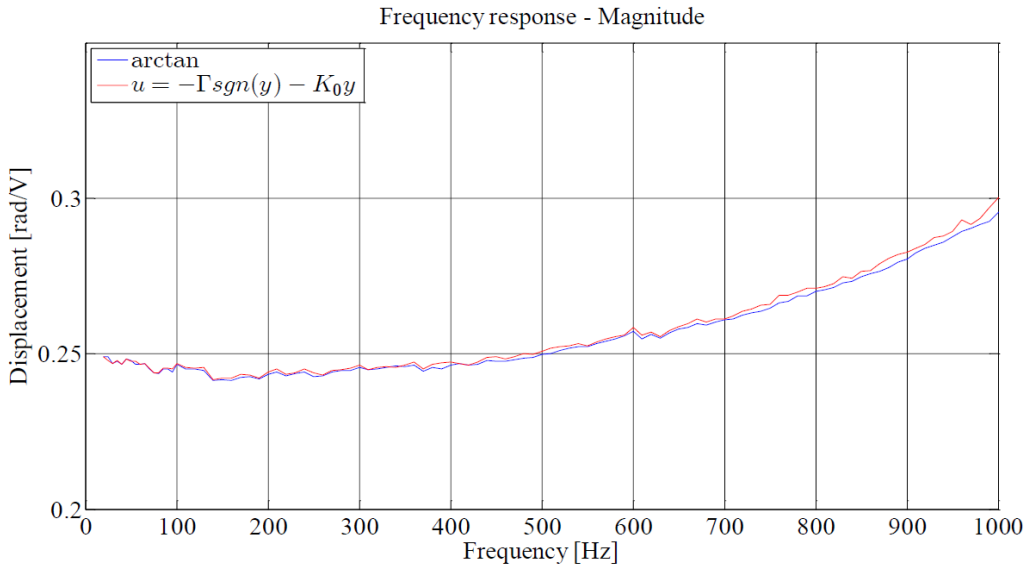


Source: from the author.

As seen before (Figures 47 and 52), the magnitude of the frequency response processed using the control system agrees with the arc tangent method, also validating this variation of the system to measure the scale factor in question, consequently, measuring displacements of the PFA.

Figure 57 – Frequency Response (Phase) of the APFMA-XY: Resonant filter both inputs and arc tangent.

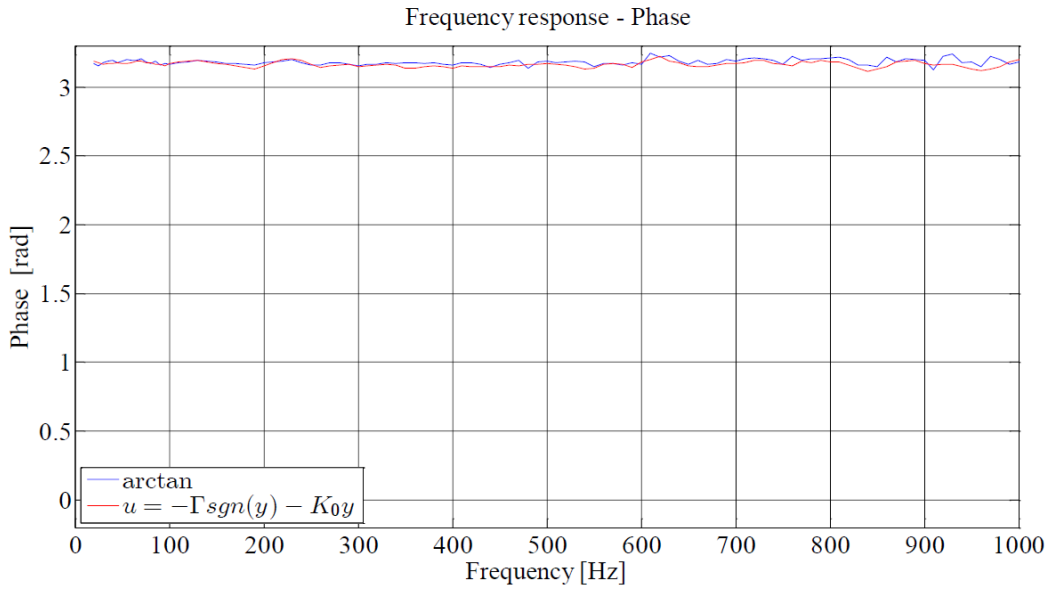


Source: from the author.

It is noteworthy to mention that the phase response in Figure 57 also follows the behavior seen in Figures 48 and 53, both methods agree within a minimal discrepancy.

The advantage of combining both inputs relies on the gain: for higher frequencies (far from the filter's resonance) the gain is in between the range of the previous systems. So, if the gain in the system is a limitation, combining this system would be a better solution to achieve higher frequencies (unless the sampling rate is not an issue, as in the analog systems, where the analog control could be project for a desired frequency, or multiple frequencies).

As in the early work about modern control applied to interferometric systems (Martin et. al, 2017; Martin, 2018; Felão, 2019), in order to smooth the response of the sign function, the sigmoidal function is presented. For this matter, the system with switching was also tested with the sigmoidal function instead of the sign function. So, the sign function can be approximated by sigmoidal function ($sigm(y) = y/(|y| + \epsilon)$. For this tests was used $\epsilon < 0.001$.

Figures 58 and 59 show the recovered total phase shift for the system working in resonance (filter and interest signal at 50 Hz, gain of $\Gamma = 200$), and out of resonance (filter at 50 Hz and interest signal at 500 Hz, gain of $\Gamma = 1{,}000$), respectively.

Figure 58 – Resonant filter with switching (sigmoidal function), operating in resonance (50 Hz, $\Gamma = 200$): Recovered total phase shift.

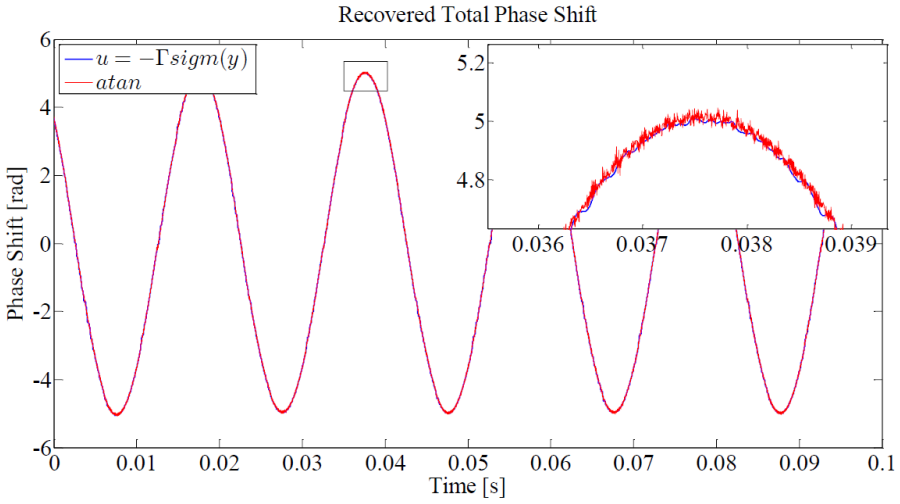


Source: from the author.

When in resonance (Figure 58), the system with the sigmoidal function has a smoother response to noise compared to the arc tangent method.

Figure 59 – Resonant filter with switching (sigmoidal function), operating out of resonance (signal at 500 Hz, filter at 50 Hz, $\Gamma = 1000$): Recovered total phase shift.

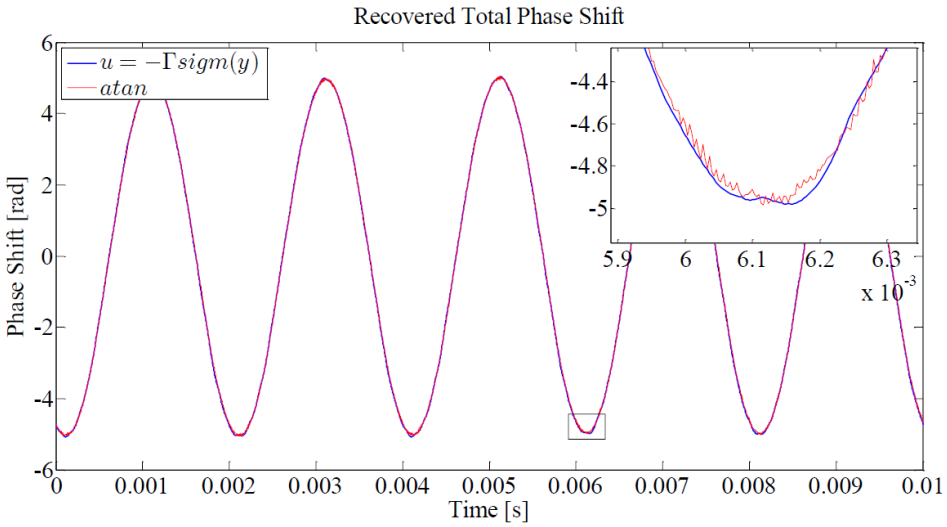


Source: from the author.

Specially out resonance (Figure 58) the recovered phase is smoother than the arc tangent classic method and the previous ones. Once the change in the switching (from the signal to the sigmoidal function) helps mitigate the chattering effect, we observe less oscillations' in Figure 59, than we have in Figure 46 for instance. This also helps to reduce the error of the measurements. To demonstrate that, the PFA frequency response was also taken.

Figure 60 – Frequency Response (Magnitude) of the APFMA-XY: Resonant filter with sigmoid and arc tangent.

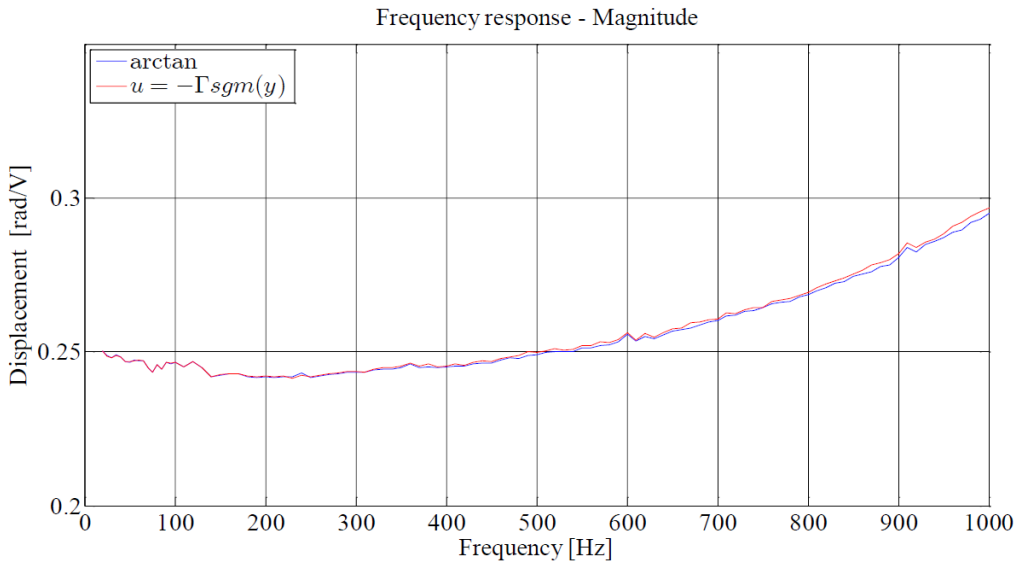


Source: from the author.

Figure 61 – Frequency Response (Phase) of the APFMA-XY: Resonant filter with sigmoid and arc tangent.

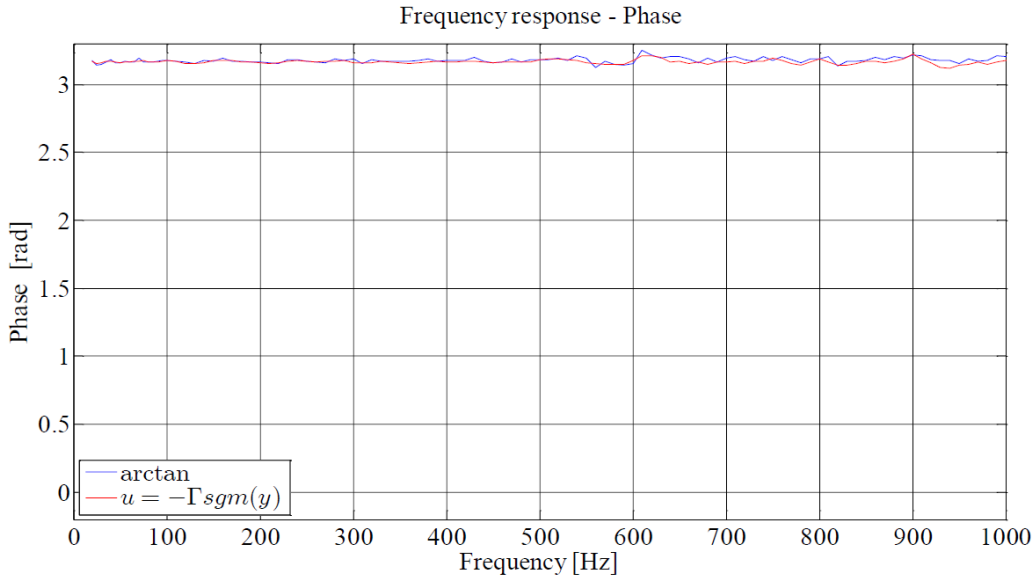


Source: from the author.

Figures 60 and 61 show that the response taken using the sigmoidal function agrees with the arc tangent method. Also, that the sigmoid has reduced discrepancies. To illustrate that, we compare all the frequency responses taken using the resonant filter systems: we have Figure 62 with all the plots and Figure 63 with the discrepancy between the control systems and the classical arc tangent method.

Figure 62 – Frequency Response of the PFA APFMA-XY for the resonant filter systems.

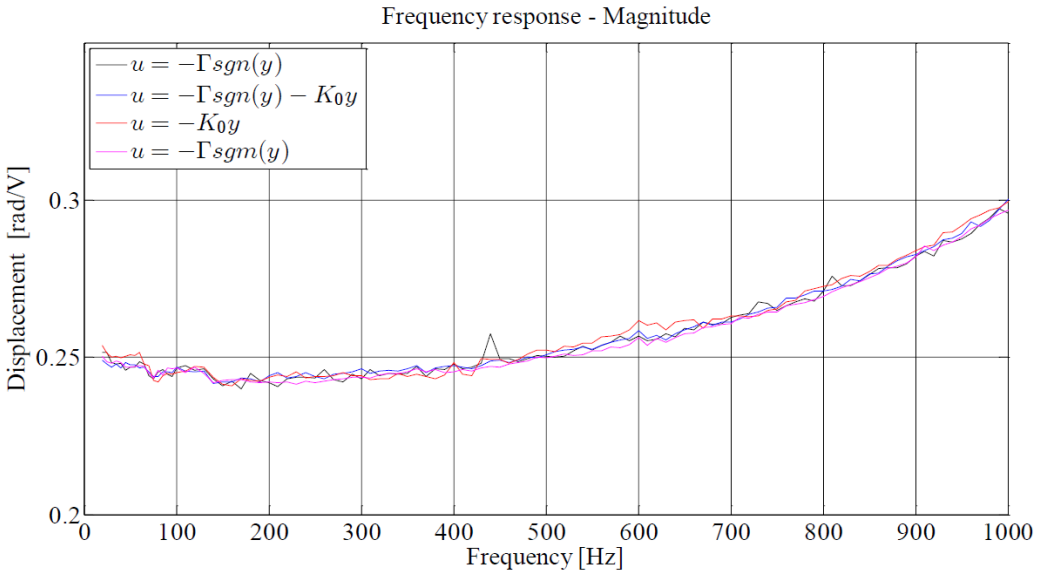


Source: from the author.

In Figure 62, besides the outliner that happens at 440 Hz when using the system with the switching only ($u = -\Gamma sgn(y)$, curve in black), all the curves have the same behavior and little discrepancy when compared to each other. Also, we can notice that for all the systems, when near the filter's resonance, the response agrees very well, yet when far the filter's resonance the difference is still acceptable. Therefore, we decided to plot the discrepancy of the system in relation to the arc tangent method, as in Figure 63.

Figure 63 – Discrepancy (%).

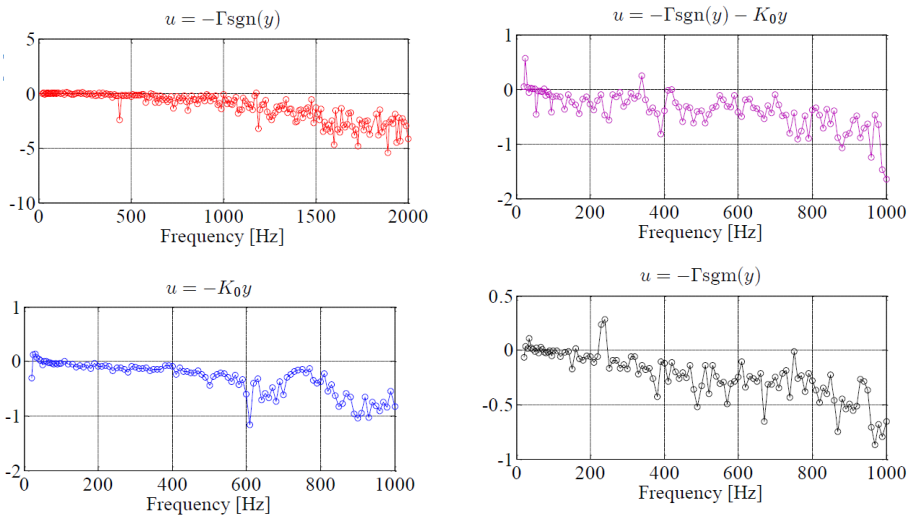


Source: from the author.

As we can see in Figure 63, the percent error is less than 5%, in general (for all the comparisons). The system with the sigmoidal function has the smaller error (less than 0.5%). When near the filter's resonance ( considering a range of $0 < f < 300\ Hz$), we observe that the error is less than 0.5% for all the cases. In general, the discrepancy being this little we can highlight that the methods implemented to achieve this results have their peculiarities: the nonlinear control doesn't mask the dynamics of the nonlinear plant such as the interferometer, which casually happens when we apply classical methods such as the arc tangent.

# 5 CONCLUSION AND FUTURE WORK

The variable structure is an elegant solution for the control and stabilization of the two beam optical interferometer. Along with it, the sliding mode brings simplicity of implementation, lowering costs and robustness. It is noteworthy that none of the methods studied, need the interferometer to be in quadrature, unless when using the virtual interferometer on the implementation of the method.

The resonant control, this new approach, looks promising due its high accuracy and robustness (for the systems with switching). One can conclude that all the resonant systems tested do work and assure the simulations and theory developed in this work. All the system variations seem to work with little discrepancy when compared to the arc tangent method. Whereas the system with sigmoidal function is smoother than the other and has the smallest error (as foreseen already being said in such applications (MARTIN, 2018; FELÃO, 2019)).

Also, we can notice that the resonant filter has characteristic of filtering a specific frequency with very high gain, there goes an advantage of working in resonance, which could be a powerful substitution on procedures to measure really small displacements. Also, since in resonance the gain of the filter goes to infinite and during the switching, the signal function also has an infinite gain, this brings a capability of full compensation (high gain approach) with a lower range of controller gain than studied before.

On the developing of this research we could evaluate the advantages and issues that the high gain approach brings. It is an approach with easy results, once the correction phase is always proportional to the interest signal. But, the fact that it needs to compensate a composed signal come with some issues: it can be a problem for processing (when working with a real-time implementation), since it ends up needing a higher sampling rate or can be limiting in gain by an analogic circuit. Also, closing a physical feedback loop is a bit challenging due the hardware available. And the risk of vibrating the feedback PZT to physical damage, reducing the frequency range that the control systems can compensated safely and out of instability (to operate in higher frequencies, it needs a higher gain generating chattering and amplifying vibrations in the PZT of feedback).

For future works, a solution for the issues presented is to implement the systems using analog circuits, or a platform with a close sampling rate (such as FPGA), allowing the system to have a physical feedback, or even using the virtual method proposed by Felão (2019). Each case comes with advantages of increasing the sampling rate and disadvantages due the

peculiarities of the methods. Also, the resonant system with both inputs could be test using the sigmoidal function instead.

In conclusion the resonant control system comes with the advantages of the high gain approach, without the need of the interferometer quadrature (when implemented using a physical feedback), as the high gain proposed by Felão (2019), and relies on small errors and smaller gains specially when operating in resonance.

# BIBLIOGRAPHY

BARBOSA. F. A. A.; NADER, G.; HIGUTI, R. T.; KITANO, C.; SILVA, E. C. N. A simple interferometric method to measure the calibration factor and displacement amplification in piezoelectric flextensional actuators. **Controle & Automação**, Heidelberg, v. 21, n. 6, p. 577-587, 2010.

CHEN, X. H.; ZENG, X. L.; FAN, D.; LIU, Q. C.; BIE, B. X.; ZHOU, X. M.; LUO, S. N. Note: Phase retrieval method for analyzing single-phase displacement interferometry data, **Review of Scientific Instruments**, Melville, v. 85, n. 026106, p. 4 , 2014.

CHEUNG, D.C.L., BARNES, T.H., AND HASKELL, T.G. Feedback interferometry with membrane mirror for adaptive optics. **Optics Communications**, Amsterdam, v. 218, p.33–41, 2003.

DEBNATH, S. K.; KOTHIYAL, M. P.; KIM, S. W., Evaluation of spectral phase in spectrally resolved white-light interferometry: Comparative study of single-frame techniques. **Optics and Lasers in Engineering**, London, v. 47, p. 1125–1130, 2009.

DECARLO, R. A.; ZAK, S. H.; MATTHEWS, G. P. Variable structure control of nonlinear multivariable systems: a tutorial. **Proceedings of the IEEE**, New York, v. 76, p.212–232, 1988.

DEVASIA, S.; ELEFTHERIOU, E.; MOHEIMANI, S. O. R. A survey of control issues in nanopositioning. **IEEE Trans. Control Syst. Technol.,** Piscataway, v. 15, n. 5, p. 799– 823, 2007.

FELÃO, L. H. V. Thesis: High gain approach and sliding mode control applied to quadrature interferometer. UNESP, Ilha Solteira, 2019.

GALETI, J. H. **Medição interferométrica de fase óptica através do método de segmentação do sinal amostrado**. 2011. 115 f. Masters dissertation (Ph.D grade in Electrical Engineering) – Faculdade de Engenharia, Universidade Estadual Paulista - UNESP, Ilha Solteira, 2011.

GALETI, J. H.; BERTON,P. L.; KITANO, C.; HIGUTI, R. T.; CARBONARI, R. C.; SILVA, E. C. N. Wide dynamic range homodyne interferometry method and its application for piezoactuators displacement measurements. **Applied Optics**, Washington, v. 52, n. 28, p. 6919-6930, 2013.

GALETI, J. H.; HIGUTI, R. T.; SILVA, E. C. N.; KITANO, C. Nanodisplacement measurements of piezoelectric flextensional actuators using a new interferometry homodyne method. **IEEE Transactions on Instrumentation and Measurement**, Piscataway, v. 64, n. 5, p. 1256-1265, 2015a.

GALETI, J. H.; KITANO, C.; CONNELLY, M. J. Improved synthetic-heterodyne Michelson interferometer vibrometer using phase and gain control feedback. **Applied Optics**, Washington, v. 54, n. 35, p. 10418-10424, 2015b.

HARIHARAN, P. **Basics of interferometry**. San Diego: Academic Press, 2007.

ITKIS, U. **Control systems of variable structure**. Jerusalem: Israel Universities, 1976.

LEÃO, J. V. F. **Interferometria óptica aplicada à medição de amplitudes de vibração nanométricas em piezoatuadores flextensionais**. 2004. Dissertação (Mestrado em engenharia elétrica) – Faculdade de Engenharia de Ilha Solteira, Universidade Estadual Paulista, Ilha Solteira, 2004.

LE LETTY, R.; CLAEYSSEN, F.; BARILLOT, F.; LHERMET, N. Amplified piezoelectric actuators for aerospace applications. *In*: PROCEEDINGS OF THE AMAS WORKSHOP ON SMART MATERIALS AND STRUCTURES–SMART. **Proceedings** [...] [*S. l.: s.n.*], 2003. v. 3, p. 51–62.

LEMES, A. S. **Novas configurações de interferômetros de quadratura e de técnicas de detecção de fase óptica baseadas em phase unwrapping**. 2014. 146 f. Dissertação (Mestrado em Automação) - Faculdade de Engenharia, Universidade Estadual Paulista - UNESP, Ilha Solteira, 2014.

MARÇAL, L. A. P.; LEÃO, J. V. F.; NADER, G.; HIGUTI, R. T.; KITANO, C.; SILVA, E. C. N. Analysis of Linearity and Frequency Response of a Novel Piezoelectric Actuator Using a Homodyne Interferometer and the J1- J4 Method. **IEEE Transactions on Instrumentation and Measurement**, Piscataway, v. 56, p. 954-961, 2007.

MARÇAL, L. A. P. **Novas técnicas de detecção de fase óptica em interferômetros homódinos aplicadas à caracterização de atuadores piezoelétricos flextensionais**. 2008. Tese (Doutorado em engenharia elétrica) – Faculdade de Engenharia de Ilha Solteira, Universidade Estadual Paulista, Ilha Solteira, 2008.

MARÇAL, L. A. P.; HIGUTI, R. T.; KITANO, C. A simplified and higher dynamic range version of the J1 J4 method for optical phase measurements, **Microwave and Optical Technology Letters**, Hoboken, v. 54, p. 387-392, 2012a.

MARÇAL, L. A. P.; KITANO, C.; HIGUTI, R. T.; NADER, G.; SILVA, E. C. N. A high dynamic range method for direct readout of dynamic phase change in homodyne interferometers. **Measurement Science & Technology**, Bristol, v. 23, p. 1-12, 2012b.

MARTIN, R. I. **Nonlinear control system based on variable structure and sliding modes for two beam optical interferometry**. 2018. 127 f. (PhD Thesis) - Faculdade de Engenharia, Universidade Estadual Paulista - UNESP, Ilha Solteira, 2018.

MARTIN, R. I.; SAKAMOTO, J. M. S.; TEIXEIRA, M. C. M.; MARTINEZ, G. A.; PEREIRA, F. C.; KITANO, C. Nonlinear control system for optical interferometry based on variable structure control and sliding modes. **Optic Express**, [*s. l.*], v. 25, p. 6335-6348, 2017.

MENEZES, J. P. C. **Análise teórica e experimental de um método interferométrico de detecção de fase óptica auto-consistente e com elevada faixa dinâmica, aplicado à caracterização de atuadores piezoelétricos flextencionais**. 2009. 147 f. Tese (Mestrado em Engenharia Elétrica) – Faculdade de Engenharia, Universidade Estadual Paulista - UNESP, Ilha Solteira, 2009.

NIEZRECKI, C.; BREI, D.; BALAKRISHNAN, S.; MOSKALIK, A. Piezoelectric actuation: state of the art. **The shock and vibration digest**, Sage, v. 33, n. 4, p. 269–280, 2001.

NATIONAL INSTRUMENTS. **Programação gráfica**. [*S. l.: s. n.*], 2015. Disponível no endereço: http://www.ni.com/getting-started/labview-basics/pt/dataflow. Acesso em: 10 fev. 2020.

SHEEM, S. K.; GIALLORENZI, T. G.; KOO, K. Optical techniques to solve the signal fading problem in fiber interferometers. **Applied Optics**, Washington, v. 21, n. 4, p. 689-693, 1982.

UDD, E.; SPILLMAN, W. B. J. **Fiber optic sensors**: an introduction for engineers and scientists. New York: Wiley, 2011.

UTKIN, V. I. **Sliding modes and their application in variable structure systems.** Moscow: MIR, 1978.

YIMNIRUN, R.; MOSES, P. J.; MEYER JR., R. J.; NEWNHAM, R. E. A single-beam interferometer with sub-ångstrom displacement resolution for electrostriction measurements, **Measurement Science and Technology**, Bristol, v. 14, p. 766-772, 2003.